Directed evolution of artificial repeat proteins as habit modifiers for the morphosynthesis of (111)-terminated gold nanocrystals

Journal:	*ACS Nano*
Manuscript ID	Draft
Manuscript Type:	Article
Date Submitted by the Author:	n/a
Complete List of Authors:	Prasad, Janak; CNRS, CEMES UPR 8011 - NanoSciences Group Viollet, Sébastien; IBBMC, I2BC, CEA, CNRS, Univ. Paris-Sud Gurunatha, Kargal; CNRS, CEMES UPR 8011 - NanoSciences Group Urvoas, Agathe; IBBMC, I2BC, CEA, CNRS, Univ. Paris-Sud Fournier, Agathe; CNRS, CEMES UPR 8011 - NanoSciences Group Valerio-Lepiniec, Marie; IBBMC, I2BC, CEA, CNRS, Univ. Paris-Sud Marcelot, Cécile; CNRS, CEMES UPR 8011 - NanoSciences Group Baris, Bulent; CNRS, CEMES UPR 8011 - NanoSciences Group Minard, Philippe; IBBMC, I2BC, CEA, CNRS, Univ. Paris-Sud Dujardin, Erik; CNRS, CEMES UPR 8011 - NanoSciences Group

SCHOLARONE™
Manuscripts

1
2
3
4
5
6
7
8
9
10
11
12
13
14
15
16
17
18
19
20
21
22
23
24
25
26
27
28
29
30
31
32
33
34
35
36
37
38
39
40
41
42
43
44
45
46
47
48
49
50
51
52
53
54
55
56
57
58
59
60

Directed evolution of artificial repeat proteins as habit modifiers for the morphosynthesis of (111)-terminated gold nanocrystals

Janak Prasad,[a, ‡] Sébastien Viollet,[b, ‡] Kargal L. Gurunatha,[a] Agathe Urvoas,[b] Agathe C. Fournier,[a] Marie Valerio-Lepiniec,[b] Cécile Marcelot,[a] Bulent Baris,[a] Philippe Minard [b] * and Erik Dujardin [a] *.

[a] CEMES, CNRS UPR 8011, 29 rue J. Marvig, B.P. 94347, F-31055 Toulouse, France

[b] Institute for Integrative Biology of the Cell (I2BC), CEA, CNRS, Univ. Paris-Sud, Université Paris-Saclay, 91198, Gif-sur-Yvette Cedex, France.

KEYWORDS: αRep proteins, anisotropic gold nanoparticles, phage display screening, Au (111) selectivity.

ORCID numbers: J Prasad: 0000-0001-6734-8747; KL Gurunatha: 0000-0001-9872-

5429; A Urvoas: 0000-0002-6077-859X; M Valerio-Lepiniec: 0000-0002-9940-0957; C

Marcelot : 0000-0002-1562-6802; E Dujardin: 0000-0001-7242-9250.

ABSTRACT. Natural biocomposites are shaped by proteins that have evolved to

interact with inorganic materials. Protein directed evolution methods which mimic

Darwinian evolution have proven highly successful to generate improved enzymes or

therapeutic antibodies but have rarely been used to evolve protein-material interactions.

Indeed, most reported works have focused on short peptides and a wide range of

oligopeptides with chemical binding affinity for inorganic materials have been uncovered

by phage display methods. However, their small size and flexible unfolded structure

prevent them to dictate the shape and crystallinity of the growing material. In the

present work, a specific set of artificial repeat proteins (αRep), that exhibit highly stable

3D folding with a well-defined hypervariable interacting surface, is selected by directed

evolution of a very efficient home-built protein library for their high and selective affinity

for the Au(111) surface. The proteins are built from the extendable concatenation of

self-compatible repeated motifs idealized from natural HEAT proteins. The high-yield

synthesis of Au(111)-faceted nanostructures mediated by these αRep demonstrates

their chemical affinity and structural selectivity that endow them with high crystal habit

modification performances. Importantly, we further exploit the protein shell

spontaneously assembled on the nanocrystal facets to drive protein-mediated colloidal

self-assembly and on-surface enzymatic catalysis. Our method constitutes a generic

tool for producing nanocrystals with determined faceting, superior biocompatibility and

versatile bio-functionalization towards plasmon-based devices and (bio)molecular

sensors.

Natural protein evolution is remarkably efficient to foster the emergence of specific

interactions between proteins and targeted molecules [1] or biomineral surfaces.[2-3]

Indeed, most inorganic structures found in living organisms such as diatom cell wall,

magnetosome, sea urchin spicule, nacre, to cite a few, are shaped and organized at the

molecular level through the intimate interactions with proteins. The efficiency of such

molecular interactions in natural systems does not rely on prior knowledge of rules

governing interaction between polypeptides and material surfaces but rather on

combinatorial selection and optimization. Mimicking the evolutionary exploration of the

protein sequence space is therefore a promising strategy to create new proteins

endowed with new tailored interaction properties. Directed evolution approaches, that

have originally been developed and broadly used to address biological questions,[4-5] can

be a powerful tool to create new artificial proteins with specific chemical affinity and

structural selectivity for crystalline material surfaces. Surprisingly, these methods have

not yet attracted the general attention in nanomaterial sciences with the remarkable

exception of short peptides.[6-10] Oligopeptides with chemical affinity for a chosen

inorganics surfaces (for example Au,[6] ZnS,[8] Co_3O_4[11]) or, even, facet-specific adsorption

(Pt(100) vs Pt(111),[12] GaAs(100) vs GaAs(111A),[7] Au(111)[13]) have been discovered by

genetic sorting methods such as phage display or cellular display.

Remarkably, in nature, the overwhelming majority of material-specific biomolecules

are proteins, not peptides owing to the very distinct molecular recognition potential of

these two classes of molecules. Peptides are too short to have a stable hydrophobic

core and hence are usually not able to reach a stable folded tertiary structure. The

molecular recognition capacities of peptides are therefore inherently limited which

translates, for peptides selected for a high chemical affinity towards inorganic materials,

into a lack of structural selectivity. Single crystals grown in the presence of such

peptides do not exceed a few nanometers in size, involving a few tens of peptides per

crystalline facets,[12] beyond which their small size and lack of stable folding cannot

prevent serendipitous polycrystalline growth.

This intrinsic shortcoming of peptides is well established in biology and has motivated

the development of combinatorial libraries of folded proteins rather than peptides which

has had a major impact for biological applications. Antibodies possess a protein

architecture known for its versatile binding capabilities and in-vitro evolved antibodies

have revolutionized the field of targeted therapeutics.[14-15] Yet, the non-biological

applications of antibodies are severely hampered by their strong propensity to

aggregate and the low efficiency of their production in bacterial expression systems.

Phage display libraries of antibody fragments have nevertheless been successfully used

to identify proteins with binding properties for polymeric[16] or inorganic surfaces[17-19] but

the binding site of being a flexible amino-acid loop, their interaction is also essentially

driven by chemical affinity and lack structural selectivity.[19]

Unfortunately, no effective alternative approach is available to design material-binding

proteins. The trial-and-error identification of surface-binding molecules remains

essentially serendipitous [20-23] leading to some successful systems exploiting natural

globular [20, 24] and fibrillary [25-26] proteins or complex plant and microbial extracts.[27-28]

However, efficiently produced and highly evolvable artificial proteins have recently

been constructed from naturally stable proteins scaffolds.[29] Extremely efficient protein

libraries have been designed by the concatenation of self-compatible repeated motifs

idealized from natural protein families such as ankyrin, HEAT or Leucine-rich repeats.[30-32] Such artificial repeat proteins are particularly promising since their interaction surface can be extended by additional motifs without compromising the stability of the folded protein scaffold. Our goal is to extend, at the interface with inorganic nanomaterials, the directed evolution strategy so far limited to short and unstructured peptides to the growing field of artificial proteins libraries.

Here, we demonstrate a new scalable strategy whereby a library of fully folded and designable proteins is exposed to crystalline Au(111) prior to the identification of the selected proteins and their use as habit modifiers in a seed-mediated nanocrystal growth approach. Robustness, to favor epitaxial facet binding, and chemical diversity, to optimize the affinity towards the chosen material, are successfully combined by exploiting the stable and rigid artificial alpha helical repeat (αRep)[33] that comprise a fixed rigid multi-α-helical scaffold and a binding surface with random sequence changes in designed positions.[33-35] This variable surface is optimized, without altering the global protein structure, for the specific binding of the non-biological Au(111) target by
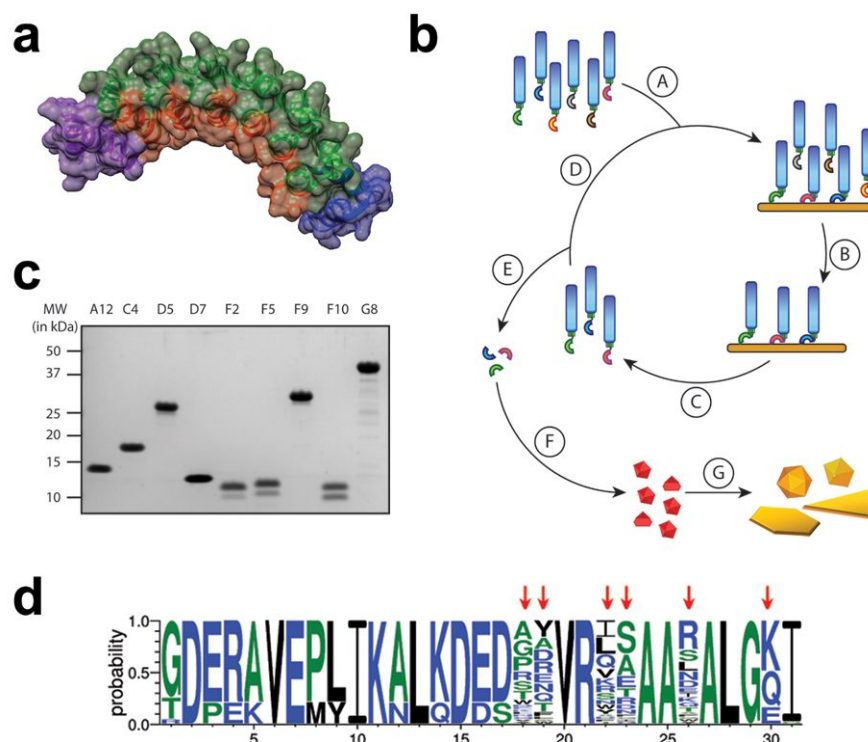
evolutionary selection and therefore offers a unique possibility for an optimal design of

gold nanocrystal habit modifiers.[31] Importantly, the selection is performed against

atomically smooth, (111)-oriented gold surface unlike peptides and protein selections

which are usually performed against polycrystalline[9, 19] or amorphous [6, 21] inorganic

targets leading to material- but not facet-specific biomolecules. The selected αReps

govern efficiently the synthesis of purely (111)-faceted crystals. Additionally, the

presence of the capping proteins enable the directed self-assembly of stacked

ensembles and satellites superstructures, or the surface confinement of enzymatic

production of electroactive species.[36]

8

RESULTS AND DISCUSSION

Selection of anti-Au(111) αRep by αRep protein phage display. The native structure of

αRep proteins is illustrated in Figure 1a and consists in the concatenation of internal

repeats composed of two antiparallel α-helices. The first (N-cap) and last (C-cap) motifs

have a similar topology but their sequence is adapted to shield the hydrophobic core.

The internal repeats comprise 31 amino-acids (AA) were defined by sequence analysis

of a group of homologous HEAT-like repeat proteins found in thermophilic organisms.[33]

The resulting consensus sequence combines twenty-five highly conserved positions

(green region in Fig. 1a) that ensure the robust structure of the folded αRep proteins

with six specific hypervariable positions that can accommodate a wide range amino acid

substitutions. Interestingly, all the hypervariable positions are gathered in the same

concave surface of the proteins (brown region in Fig. 1a) allowing to choose them in

order to confer the proteins specific interaction properties.[34] To exploit the combined

asset of structural robustness and functional interaction specificity of these proteins, we

have built a large combinatorial phage library of αReps distinct from each other by (i)

the number of internal repeats and (ii) the random nature of the AA in the hypervariable

positions.[34] Such a library of $1.7x10^9$ unique clones is sufficiently diverse to allow

selection of new αRep proteins binding tightly and specifically to almost any other

protein defined *a priori*. The αRep library was initially developed for biological

applications such as the generation of crystallization chaperones,[37] cell tracking[38] or in

protein interference experiments.[39] In this work, we apply it, for the first time, to optimize

the protein-metal surface affinity and to identify αRep proteins that can act as habit

modifiers for the growth of crystalline gold nanoparticles by strong and specific

adsorption to pre-determined Au(111) crystal facets.

Figure 1. Construction and directed evolution of Au(111)-binding artificial repeat proteins. (a) 3D representation of the crystallographic structure of a 4-repeat αRep protein depicting the internal repeats comprising the hypervariable positions (brown) with their conserved scaffold regions (green), N- and C-cap (blue). (b) Schematic flowchart showing the phage display design and selection of αRep's (A-D) and the αRep directed Au nanocrystal morphosynthesis (I-J) process. These steps involve: (A) Construction of the phage display library; (B) αRep selection on planar Au(111) substrate on mica and elution of unbound phage at pH5; (D) acid elution of Au-bound phages and bacterial amplification of selected phages (E) proteolytic isolation of αRep from phage body and large scale production. The morphosynthesis of Au nanocrystals by seeded growth process comprises: (F) αRep directed Au seed synthesis; (G) nanocrystal growth in the presence of excess αRep through hydroxylamine-mediated disproportionation mechanism. (c) Coomassie blue stained SDS-PAGE profiles of 9 different Au(111)-selected αRep after cleavage digestion. The position of the major bands represents the molecular weight of respective αRep. (d) Sequence logo obtained

by multi-alignment of the sequences of all the repeats from the selected αRep, including those of the N-cap that have the same second helix as the internal repeats, hence the apparent variability observed in positions (1,3,4,8,9,12,14,17). The binding hypervariable surface is generated by the position indicated by red arrows.

First, αReps with high affinity for Au(111) surface are selected by exposing the

combinatorial phage library to a planar Au(111) film and following the steps depicted in

Figure 1b (See Materials and Methods and Section A in Supplementary Information).

The phage population bearing αReps is incubated at pH 7.5 with freshly prepared

Au(111) surfaces (Step A). Weakly bound phages are eluted (Step B) while the

Au(111)-bound clones are collected by acidic elution (Step C) and amplified in bacteria

(step D). This iterative biopanning procedure was repeated three time before 96

Au(111)-interacting clones were randomly picked from the emerging sub-population,

expressed, isolated and tested by standardized ELISA assays against similar freshly

prepared Au(111) substrates (See Supplementary Information Figure S1a). 18 clones

showed positive ELISA response, however after sequencing a total of 9 different

Au(111)-binders with internal repeat numbers (n) comprised between 1 and 10 and pI

ranging from 5.3 to 9.05 were identified and will be labeled A12, C4, D5, D7, F2, F5, F9,

1
2
3
4
5
6
7
8
9
10
11
12
13
14
15
16
17
18
19
20
21
22
23
24
25
26
27
28
29
30
31
32
33
34
35
36
37
38
39
40
41
42
43
44
45
46
47
48
49
50
51
52
53
54
55
56
57
58
59
60

F10, G8 in the following (Fig. S1). The chemical diversity of the hypervariable positions

(Figure 1d) indicates that the interaction between the protein and the Au(111) surface is

complex and does not yield a single optimal configuration. Yet, the selected

hypervariable AA are the same as the AA found in non-thiolated gold-binding

polypeptides.[6, 13] Recent modeling of the peptide-Au interface have indeed shown that

optimal adsorption could be attained with sp^2 conjugated (Trp, Tyr, Arg), polar (Gln,

Asn, Ser), positively (Arg, Lys) and negatively (Glu, Asp) charged amino acids, thus

suggesting a large variety of possible adsorption scenarii for gold-binding proteins.[40-43]

The molecular weight of the proteins ranges between 12 and 42 kDa as shown in the

SDS-PAGE profile shown in Figure 1c and correspond to 1 to 10 internal repeats. The

large size variation of the selected αReps is also consistent with the concomitance of
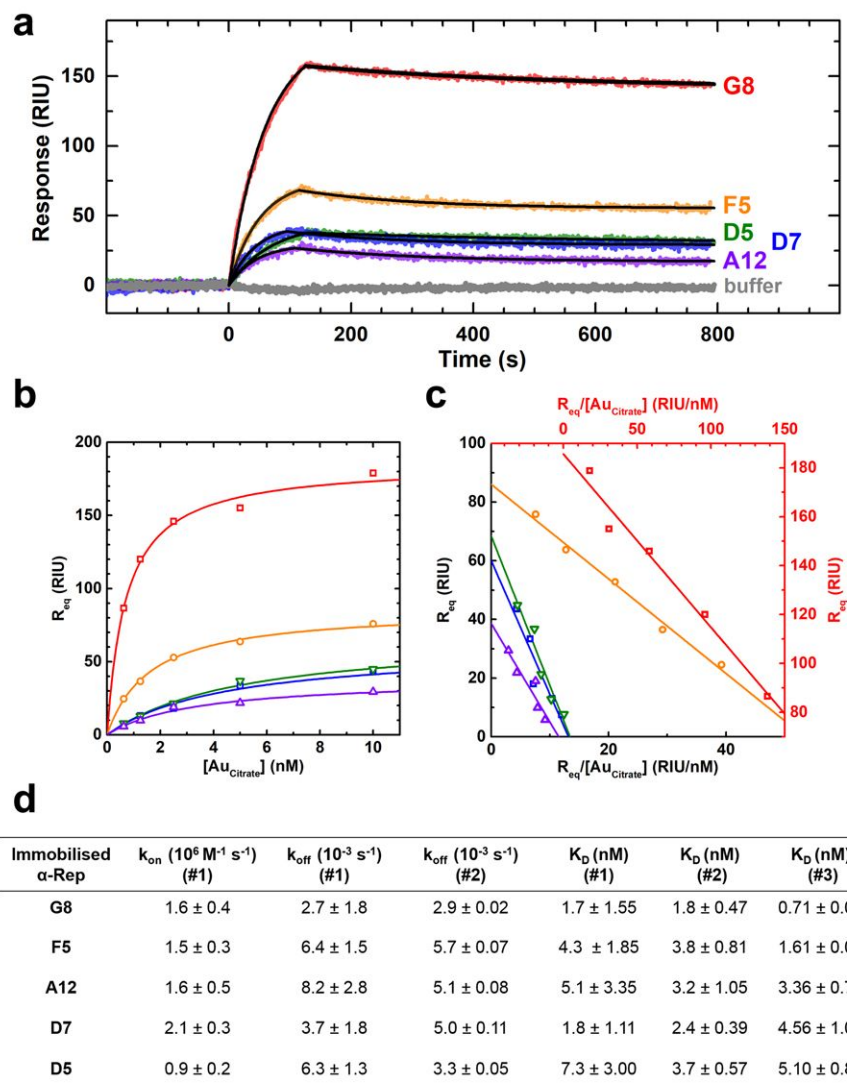
several different gold-binding mechanisms.

SPR characterization of the gold affinity of the selected proteins. To further assess the

gold-binding specificity and estimate the affinity constants, each of the nine binders was

immobilized on Surface Plasmon Resonance (SPR) sensor chips and subjected, first, to

a high influx of citrate-stabilized, decahedral gold nanoparticles exposing primarily (111)

facets[44] and, second, to an influx of pure buffer, as described in Materials and Methods.

The sensograms for A12, D5, D7, F5 and G8 and buffer are shown in Figure 2a (See

also Supplementary Information Figure S2a for C4, F9, F10, F2 and extra controls). A

significant positive association phase is observed, which shows a maximal response for

G8 followed by F5, D5, D7 and, at a lower level, by A12. When the nanoparticles bound

to the protein-coated substrates are washed with a pure buffer a small reduction of the

SPR response is observed indicating that some dissociation occurs leading, in first

approximation, to a new equilibrium state. No association is observed during control

experiments performed either by replacing the Au nanoparticle with buffer during the

initial influx or by immobilizing an αRep protein of identical structure but with no specific

affinity for gold such as a GFP-binder with 4 internal repeat (bGFPa).[34] The maximal

SPR response is observed with the largest protein containing 10 internal repeat (G8). A

control sensogram was performed with a non-selected αRep with 10 internal repeats

(N10) and is shown in Figure S2a. The low binding signal observed for N10 is clearly

marginal compared to the one of G8, which precludes the control of the protein-gold

surface simply by the protein size and confirms the role of the AA selection in the

variable positions. The general behavior indicates that G8, F5, D5, D7 and A12 gold-

binding proteins have the ability to capture citrate-stabilized gold nanoparticles, while

the other proteins show no significant detectable affinity during SPR tests. More

quantitative insight can be gained by extracting dissociation constants from the

sensograms using the three approaches detailed in the supplementary section (Section

S2). The first dataset (K_D#1) is derived from the kinetic constants of the association

phase, k_{on} and $k_{off\#1}$ (Figure 2d). The second dataset (KD#2) takes into account the

corrected $k_{off\#2}$ values from the dissociation phase.

Figure 2. Gold affinity of the selected anti-Au(111) repeat proteins. (a) SPR sensograms during adsorption and desorption phases monitoring the interactions between immobilized αRep proteins (see labels) and citrate-stabilized Au nanoparticles ([Au_{cit}]=10 nM). Solid black lines are exponential fits to the association and dissociation phases. The exponent of the association fits provides the association (k_{ON}) and dissociation (k_{OFF} #1) kinetic constants tabulated in (d). The dissociation phase fits provide the k_{OFF} #2 kinetic constant in Table (d). Each protein data is associated to the same color throughout the figure. **(b)** SPR equilibrium analysis along with Langmuir fits (continuous lines). **(c)** Scatchard plot for the empirical estimation of the dissociation

constants labelled K_D #3 which is obtained from the slopes of the linear fits. G8 data (red) are plotted on the red x-y axis while all other data share the black x-y axis. **(d)** Summary table of all association (k_{ON}) and dissociation (k_{OFF} #1 and k_{OFF} #2) alongside the dissociation constant (K_D) values obtained from the ratio of kinetic constants (K_D#1= k_{OFF} #1 / k_{ON}, K_D#2= k_{OFF} #2 / k_{ON}) and from the Scatchard plot (K_D#3).
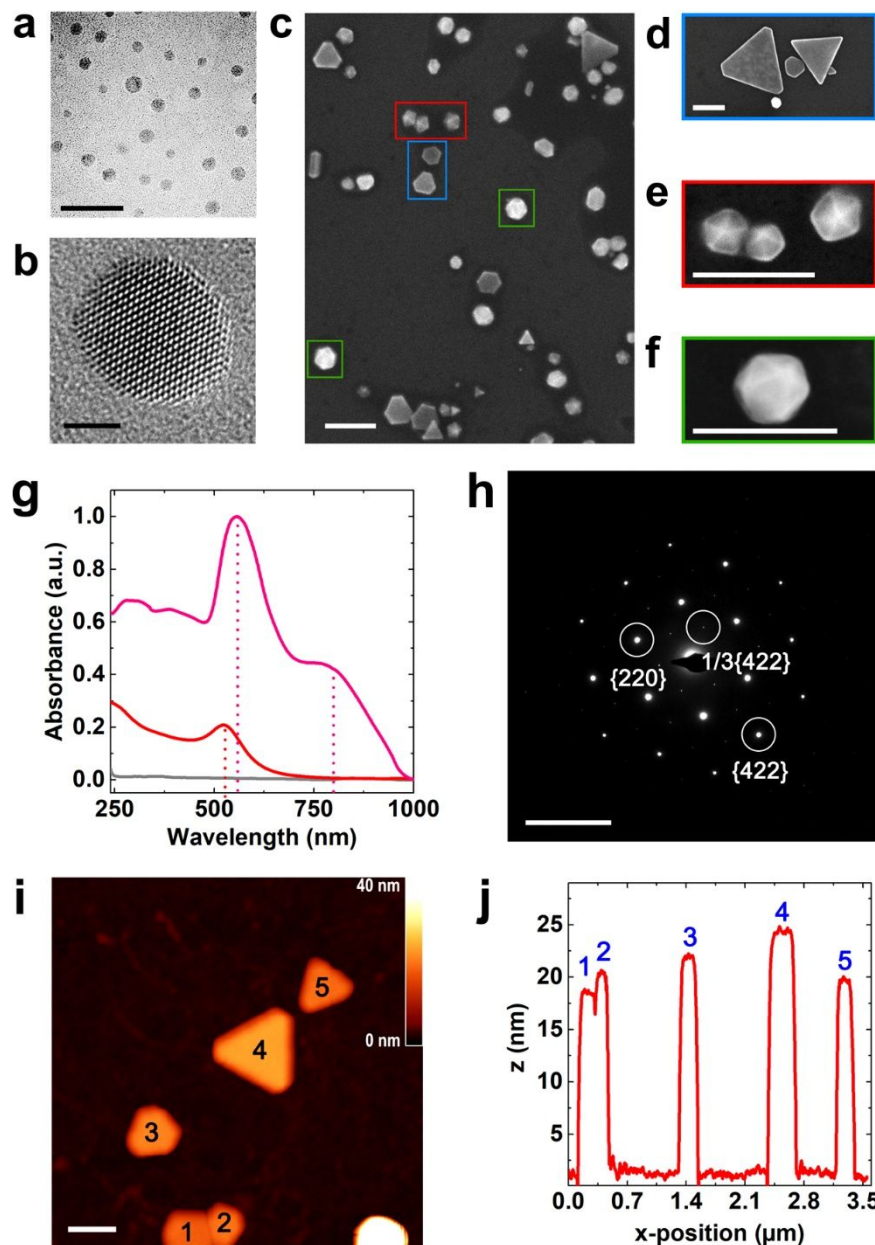
The third dataset (KD#3) is obtained by fitting the data with the Langmuir isotherm

model (Figure 2b) followed by a Scatchard linearization (Figure 2c). All three

quantitative analyses consistently yield sub-10 nM dissociation constants similar to the

ones routinely measured in protein pairs involving at least one αRep binder.[34] This SPR

study demonstrates that the selected αRep proteins readily associate with the solid gold

surface and quantifies the Au(111)-binding strength, which is maximal for G8.

Furthermore, taking into consideration their intrinsic rigid tridimensional folded shape,

their high pH and thermal stability and their high expression potential that allows the

production of mM solutions, these proteins possess a strong potential as selective

Au(111) capping agents and even as crystal habit modifiers in the synthesis of Au

nanoparticles.

Protein-controlled nanocrystal morphosynthesis. This unique feature is revealed by

the reduction of a gold precursor in the presence of αRep-capped seeds and free αRep

which results in the morphosynthesis of protein-capped gold nanoparticles exclusively

terminated with (111) facets (Figure 1b, steps F and G). First, gold seeds (7 ± 1 nm) are

produced by the reduction of Au^{3+} to Au^0 with an extrinsic mild reducing agent, sodium

formaldehyde sulfoxylate (SFS),[45] in a buffered (pH 7.5) solution of αRep protein acting

as capping agents (Fig. 3a and Fig. S3a). The bright red seed solution is produced

within two hours after SFS addition, ten times faster than known protein-free methods,[20-

21, 24] probably thanks to the stabilization by the protein capping. The seeds are

crystalline with frequent single or penta twin boundaries and occasionally polycrystalline

(Fig. 3b and Figs. S3d-h). The presence of a protein shell is confirmed by a 7-nm red

shift of the plasmon resonance peak of the αRep-capped seeds compared to protein-

free seeds (Fig. S4b), by the light organic halo surrounding the Au seeds in TEM

micrographs (Fig. S3a) and by the prolonged colloidal stability with no sign of

aggregation after several months at 4°C. Furthermore, the electrophoretic mobility of

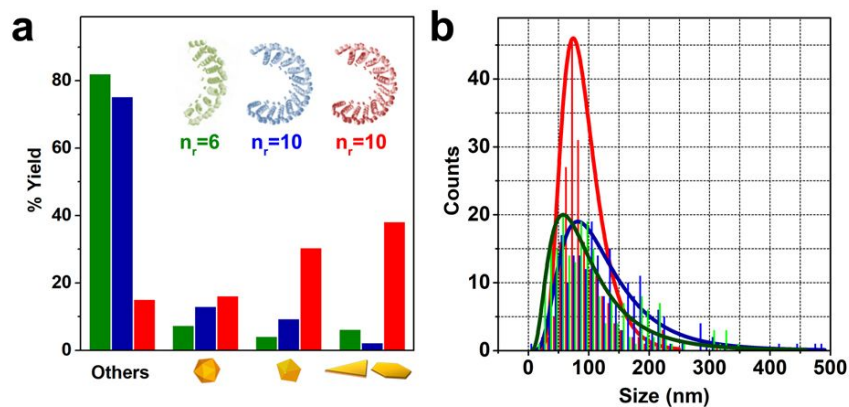seeds synthesized with any selected αRep proteins having different number of internal

repeats (n) varies consistently with the net surface charge of the corresponding protein

in pH 8.5 tris-borate buffer (Fig. S3c). In spite of the presence of the proteins, the seeds

are systematically spherical, which suggest that the proteins, at the seed stage, do not

induce faceting but merely act as surface stabilizers when the direct reduction is

performed with SFS. The seeds are then injected in a fresh solution set at pH 5 and

containing Au^{3+}, one of the selected αRep and hydroxylamine, which is not able to fully

reduce gold at this pH and in the absence of seeds (See Section S4 in Supplementary

Information).[46] The appearance of a pink-to-purple color in the different solutions

confirms the surface-mediated growth through disproportionation reaction[47] onto the

pre-formed Au seeds, as demonstrated for G8 in Figure 3 and generalized to all

selected αRep proteins in Figures 5i-l and in Sections S5 and S6 of Supplementary

Information. Detailed electron microscopic examination reveals that the resulting colloid

is composed of three (111)-terminated subpopulations of 2D nanoplates (38.2%),

decahedra (30.4%) and icosahedra (16.2%) with only 15.2% of other random structures

(Figs. 3a and 4a). The ensemble absorption spectrum of as-synthesized nanostructures

displays two peaks centered at 556 nm and 804 nm (Fig. 3b), suggesting a composite

nanocrystal population. The former one dominates and is associated to a plasmon

resonance in quasi-isotropic nanoparticles (decahedra and icosahedra). The latter peak

shouldering at 780 nm arises from the in-plane higher order plasmon modes of

prismatic nanoplates.[48] Selected area electron diffraction (SAED) patterns recorded on

the nanoplates exhibit three sets of spots of decreasing intensity that are indexed to

(220), (422) and 1/3(422) planes of fcc gold (Fig. 3c).[49] The 2D prisms are single

twinned crystals sharing the same [111] zone axis aligned with the electron beam and

thus exposing two extended (111) basal facets.

Figure 3. Morphological and structural characterization of αRep-coated, (111)-terminated Au nanocrystals. (a,b) High resolution TEM of spherical G8-stabilized seeds showing a high degree of crystallinity. The seed in (b) is single crystalline and oriented along the [011] zone axis **(c)** Representative SEM micrograph of G8-capped, (111)-facet terminated Au nanostructures showing nanoplates (blue box), decahedrons (red box) and icosahedrons (green box) morphologies. **(g)** Characteristic UV-visible spectra of G8 templated Au seeds (red, λ_{max} = 524 nm), seedless growth solution (grey) and Au nanostructures synthesized by the G8-templated, seeded growth approach (pink), which

exhibit two peaks at λ_{max} = 556 nm and λ_{max} = 804 nm. **(h)** Selected area electron diffraction of an Au nanoplate showing diffraction spots along the [111] zone axis. **(i)** Tapping mode AFM image of five Au nanoplates. **(j)** Height profile of the five nanoplates shown in (i), which all have a thickness of 21 ± 3 nm. Scale bars are (a) 20 nm, (b) 2 nm, (c-f, i) 200 nm, (h) 10 nm^{-1}.

Figure 4: Comparative analysis of nanocrystal shapes and sizes obtained in the presence of control proteins, anti-GFP and N10, or anti-Au(111) G8. (a) Histogram showing the relative occurrence of nanoprisms, decahedra, icosahedra and other shape (spheroidal, and irregular shapes) obtained by morphosynthesis with anti-GFP αRep (green), of consensus sequence N10 αRep (blue) and the isomorphic anti-Au(111) G8 αRep (red). (b) Size distribution histograms and log-normal fits of as-synthesized nanocrystals with anti-GFP (green), N10 (blue) and G8 (red) αRep proteins (200 measurements for each set).

While the lateral dimensions of the nanoplates vary between ca. 50 and 500 nm, they

show a fairly uniform thickness of 22 nm as evidenced by atomic force microscopy

(AFM) measurements displayed in Figures 3d and 3e, in good agreement with twinned

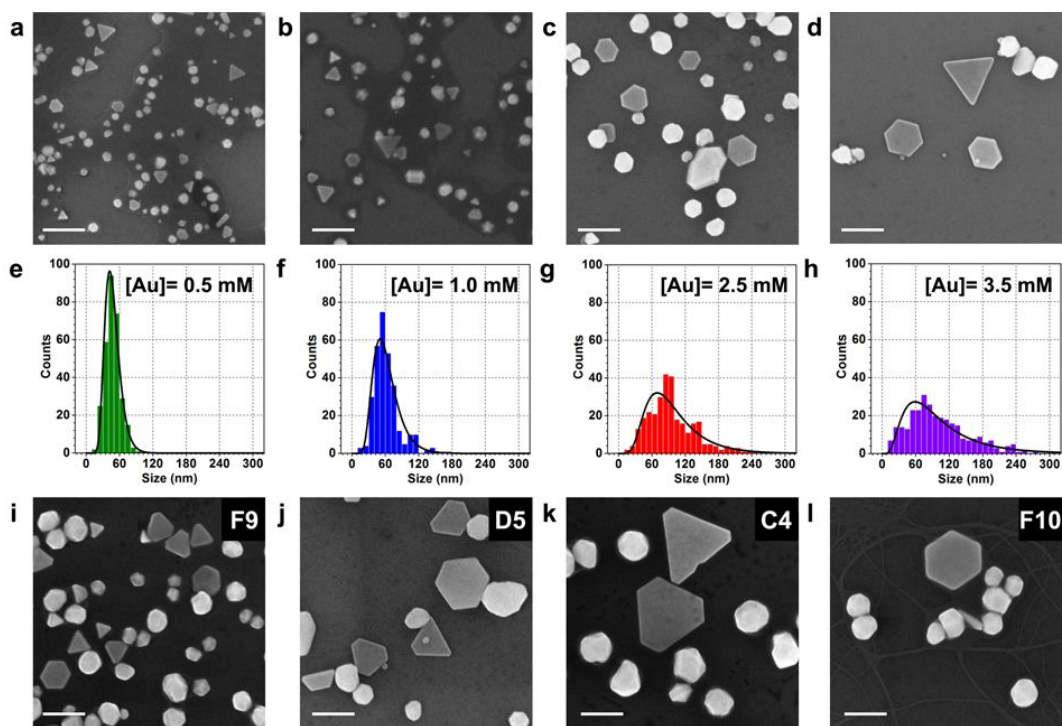nanoprisms of similar morphology produced by other methods.[50-52]

Figure 4 demonstrates that the direct effect of the facet-specific gold affinity of

Au(111)-selected G8 proteins on the morphology and structure of the gold nanocrystals

is absent for analogous proteins that have not been selected against Au(111).The exact

same synthesis conditions used with G8 in Figure 3 are performed with the two control

αRep proteins, N10 and bGFPa, that have no specific affinity for Au(111) surfaces

(Fig. S7).[34] Figure 4a clearly illustrates that the (111)-faceted nanoplates, icosahedrons

and decahedrons represent only 25% and 18% of the particles produced in the

presence of bGFP and N10 respectively while they amount to 85% when the

morphosynthesis is performed with G8. The vast prevalence of (111)-terminated

nanoparticles in the latter case results from the specific and strong binding of the

designed proteins to emerging (111) facets as the metal growth proceeds in pH

conditions similar to the one corresponding to the binding step during the protein

selection (Fig. 1, step B). The strong protein-surface affinity hinders the build-up on

(111) facets, which are thus stabilized, and results in enhanced growth rates in other

available crystallographic directions. Decahedra and icosahedra only expose (111)

facets and thus are fully coated with αRep proteins leading to a rapid inhibition of their

growth. As a consequence of the seed-mediated protocol and of the effective growth

inhibition of the (111) facets, the size distribution of the G8-driven synthesis is twice

narrower (92 nm ± 35 nm) than the two control experiments (130 nm ± 77 nm for N10

and 106 nm ± 75 nm for bGFP) as seen in Figure 4b.

Interestingly, nanoplates are formed by inhibiting the two basal (111) facets of single

twinned seeds but their edges expose (100) and (110) facets that keep growing even in

the presence of the selected proteins as witnessed by the larger edge length distribution

(Figs. 3 and 4b), which further confirms the (111) binding specificity of the selected

αRep proteins. The kinetic control obtained by performing the hydroxylamine reduction

at pH 5 allows to tune the nanocrystal size distribution by adjusting the Au^{3+} ions flux in

the growth solution. In Figures 5a-h, the G8-mediated nanocrystal synthesis is

performed with increasing Au^{3+} concentrations and shows the same types of structures

with a marked increase of the nanoplate edge length. The overall size distributions shift

from 48 ± 14 nm for $[Au^{3+}]$ = 0.5mM to 105 ± 72 nm for $[Au^{3+}]$ = 3.5mM and is

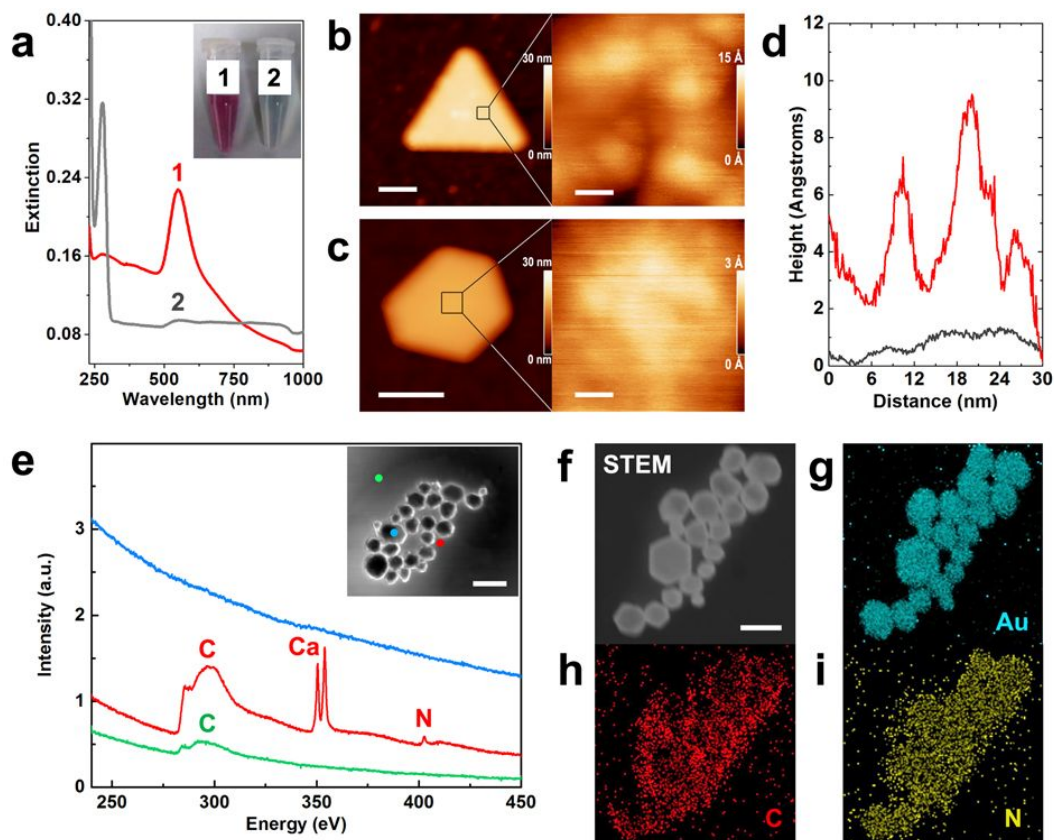accompanied by a red-shift of both plasmon resonances (Figs. S8a,b).

Figure 5: Nanocrystal size adjustment by varying the initial Au³⁺ concentration and generalized synthesis with other selected proteins. (a-h) SEM micrographs and nanocrystal size distribution of kinetically controlled G8-capped Au nanostructures for four different Au³⁺ concentrations: (a, e) 0.5 mM; (b,f) 1.0 mM; (c,g) 2.5 mM; (d, h) 3.5 mM. The histograms follow lognormal distributions (black lines) with sizes of (e) 48±14 nm, (f) 62±24 nm, (g) 99±50 nm and (h) 105±72 nm. (i-l) SEM micrographs of nanostructures synthesized in the presence of different αRep at the same Au³⁺ concentration of 2.5 mM: (i) F9; (j) D5; (k) C4; (l) F10. Scale bars: 200 nm.

This shift is more pronounced for the higher order plasmon mode peak in agreement

with the significant increase of the nanoplate edge length (from 54 ± 4 nm for

$[Au^{3+}]$ = 0.5mM to 180 ± 7 nm for $[Au^{3+}]$ = 2.5mM) compared to the moderate growth of

the spheroidal nanocrystals (from 46 ± 2 nm to 78 ± 3 nm) and the quasi negligible

thickening of the nanoplates (Figs. S8c,d). Indeed, at the lowest concentrations, the in-

plane size of the nanoplates is similar to the diameter of the decahedra and icosahedra

(Figs. 5a). However, as $[Au^{3+}]$ increases, the overall increase of mean size and size

spread is predominantly ascribed to the lateral growth of the nanoplate subpopulation,

with an in-plane size reaching ca. 3-4 times the spheroidal diameter at $[Au^{3+}]$ = 3.5mM

(Fig. 5d). This further illustrates that the (111) growth inhibition by the proteins does not

apply to other crystallographic directions, like (100) and (110). Very similar results,

albeit with specific nanocrystal size distributions, were obtained for several of the

selected proteins: F9, D5, C4 and F10 as shown, for $[Au^{3+}]$ = 2.5mM, in Figures 5i to 5l

respectively. Contrary to previous studies[20-21, 53] where pH and temperature are

commonly used to control the shape and yield of nanocrystal morphosynthesis, these

parameters have no marked influence on the growth process (see sections S9 and S10

in Supporting Information), which indicates that our approach is predominantly

determined by the effective design of the protein-gold interactions.

Structural and interfacial characterization of the protein-coated (111)-faceted

nanocrystals. Remarkably, at elevated temperatures (T > 37°C), basal stacking of

nanoplates is observed suggesting an inter-particle assembly process mediated by

interactions between proteins strongly tethered to the basal surfaces.[54] Since the direct

evidence of robust protein attachment to the nanocrystal surface is challenging for low

molecular weight proteins like αRep's (~12 - 42 kDa), we have performed a series of

analysis of the αRep-gold interface, which are gathered in Figure 6. Proteolytic

trypsinization of G8-coated gold nanocrystals was conducted by addition of 20 μM

trypsin in 0.01 M phosphate buffer at pH 8 (Fig. 6a). The originally clear red solution

(tube 1) rapidly turns grey with the appearance of a small black precipitate (tube 2) as

the proteins are degraded. This correlates to the complete disappearance of the 530 nm

plasmon peak in the absorbance spectrum. Non-contact AFM (nc-AFM) was performed

in ultrahigh vacuum (UHV) on individual nanoplates deposited onto smooth silica

substrate (Figs. 6b-d). This AFM mode is used for atomic resolution imaging and it

ensures that the proteins are not distorted during the raster scanning of the tip.

Figure 6: Chemical analysis of the αRep-Au interface on the surface of the G8-coated nanocrystals. (a) Trypsinization test on G8-capped nanocrystals monitored by UV-visible spectrometry. Sample in tube1 consists in stable nanocrystals produced with G8 that show a clear plasmon resonance at 520 nm (spectrum 1). In tube 2, trypsin is used to degrade the protein shell resulting in nanocrystal aggregation and the disappearance of the resonance peak (spectrum 2). **(b, c)** nc-AFM images of (b) G8-capped and (c) O_2 plasma cleaned nanoplates. The black squares indicate the areas zoomed in the right panels. Scale bars are 100 nm and 6 nm for the left and right panels respectively. **(d)** nc-AFM height profiles of the G8-coated triangular nanoprism (red) and of the plasma-

cleaned hexagonal nanoprisms (black) shown in (b) and (c) respectively. **(e)** EELS spectra taken from three locations in the TEM image of streptavidinylated G8-capped nanocrystals shown in inset. The background spectrum (green) shows only the carbon peak. The blue spectrum taken at the center of a Au nanocrystal shows a large uniform background due to a very low energy Au peak located out of the spectral window. The red spectrum recorded tangentially to the nanocrystal reveals the presence of Nitrogen, Carbon, and Calcium. Note that the Ca signal is ascribed from the calcium-based purification method of commercial streptavidin. Scale bar in inset is 200 nm. **(f)** STEM image and **(g-i)** corresponding EDS maps showing elemental distribution of (g) gold (h) carbon (i) nitrogen. Scale bar in (f) is 400 nm.
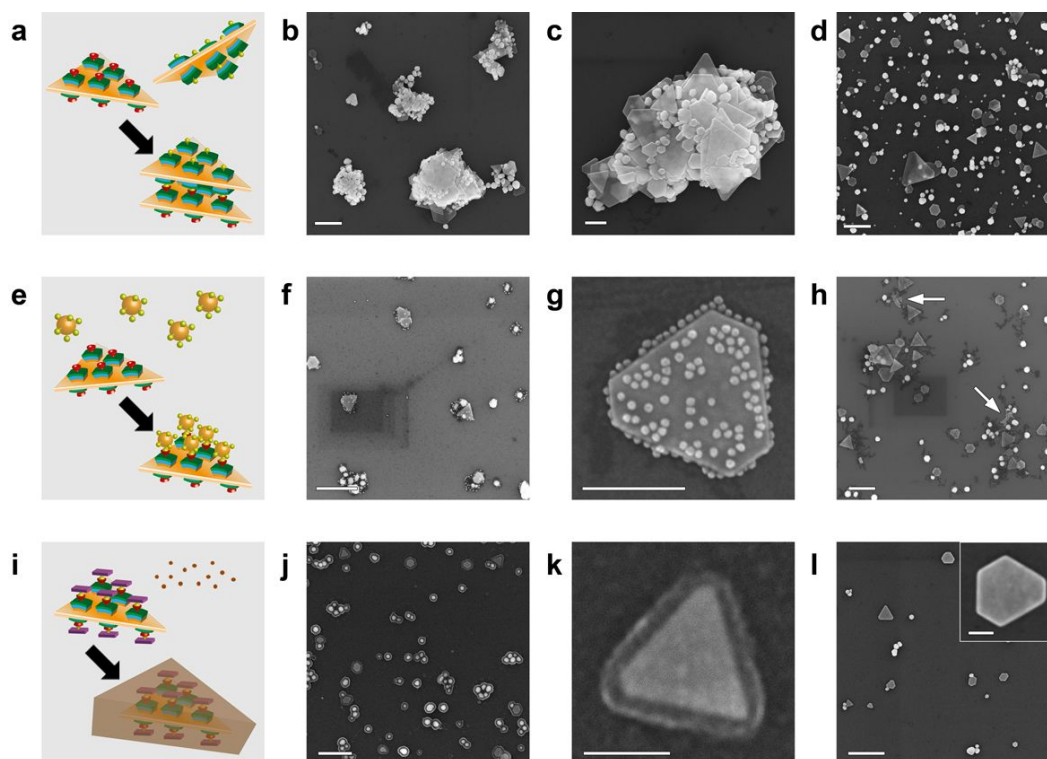
When performed on the as-synthesized nanoplates, a uniform surface is observed

which is constellated with globular objects of typical lateral sizes of 5-15 nm (Fig. 6b)

and a height corrugation of about 5-7 Å (Fig. 6d, red line). This is consistent with an

irregular protein coating surface. The sample was then treated with a r.t. O_2 plasma to

remove all organic adsorbates and re-introduced in UHV, outgassed for 24 h before

resuming nc-AFM imaging (Fig. 6c). The apparent total height of the nanoplates is

about 5 nm smaller after plasma cleaning, which is consistent with the removal of the

protein capping layer. Moreover, the upper surface is extremely smooth (Fig. 6c) with a

corrugation reduced down to 1-1.5 Å, which corresponds to atomically flat Au terraces

(Fig. 6d, black line). Similar samples drop-casted onto electron microscopy grids were

analyzed by electron energy loss spectroscopy (EELS) in the 250-450 eV energy loss

window as shown in Fig. 6e. The EELS signal from the core of the nanocrystals (cyan

spot and line) is dominated by the tail-off of the low energy peak of gold. However,

spectra recorded just on the edge of the nanocrystal (red spot and line) reveal the

peaks associated to carbon and nitrogen loss energies, as expected from a thin protein

coating. The supporting carbon film (green spot and line) only accounts for a small

fraction of the carbon signal, which can be predominantly ascribed to the proteins.

Finally, STEM/EDS elemental analysis performed on nanocrystals drop-casted onto

ultrathin SiO_2 membranes are shown in Figures 6f-i and S11. The gold (Fig. 6g), carbon

(Fig. 6h) and nitrogen (Fig. 6i) EDS maps perfectly match the STEM image with very

little background signal. Taken together, these analyses clearly demonstrate that the

nanocrystals are coated by proteins which remain on the surface after the

morphosynthesis and purification steps. We expect the hyper-variable side, which is the

only one able to discriminate the Au(111) surface during the selection process, to be

strongly interacting with the nanocrystal surface and thus probably exposing the non-

variable backside of the proteins to the surrounding medium.

Versatile functionalization of the αRep-coated nanocrystals. To fully exploit the

potential of these protein-coated nanoparticles, we use the displayed αReps as

modules to directly integrate functional bioactive elements onto anisotropic nanocrystals

without resorting to tedious ligand exchange procedures.[35] One first option is to

incorporate a secondary streptavidin (STV) layer through biotinylation of the Lys

residues present in the exposed αRep backside via the standard NHS-NH$_2$ coupling

method. This streptavidinylation of αRep offers a versatile platform to confer the gold

nanocrystals with targeted self-assembly and catalysis functionalities. The feasibility of

this approach is demonstrated in Figures 7a-c where streptavidinylated αRep gold

nanocrystals are coupled to NHS-biotin modified αRep gold nanocrystals resulting in

large 3D self-assemblies mostly driven by the face-to-face stacking of the nanoplates by

streptavidin-biotin recognition. Beyond this direct basal stacking, a detailed examination

of micrographs suggests that the platonic nanostructures, which probably exhibit

accessible biotin and streptavidin molecules on all facets, also contribute to the

crosslinking of the large assemblies and are often found inserted between nanoplates.

UV-visible spectroscopy monitoring on equimolar mixtures of streptavidinylated and

biotinylated gold nanocrystals shows a marked decrease of the plasmon resonance

peak and suggests that self-assembly occurs in solution. In the absence of biotin (bn)

on the second partner, the nanocrystals remain isolated from each other and no

aggregation is observed (Fig. 7d). This first scheme demonstrates that fully functional

αRep proteins are present on the (111) facets of nanocrystals where they can be freely

coupled to other biomolecules to create patch antenna-like stacks.[55]

Figure 7: Functional surface derivatization of αRep protein coated nanocrystals. (a) Scheme and **(b, c)** SEM images of basal stacking of G8-capped Au nanocrystals obtained by self-assembly between streptavidinylated and biotinylated nanocrystals. **(d)**

Control experiment in absence of biotin shows no stacking. **(e)** Scheme and **(f, g)** SEM images of core-satellite hybrid assemblies obtained by combining streptavidinylated G8 nanocrystals and biotin-PEG Au nanospheres which results in the decoration of the top and bottom prism facets by the nanospheres. **(h)** Control experiment with non-streptavidinylated G8-capped Au nanocrystals. No satellite is observed even though segregated nanosphere clumps can be found (white arrows). **(i)** Scheme and **(j, k)** SEM images of on-surface DAB catalysis by HRP-Biotin tagged streptavidinylated G8 nanocrystals results in a uniformly wrapping polymer corona. **(l)** Control experiment run with simply streptavidinylated nanocrystal in the absence of HRP. No polymer capping layer as shown also in the inset. Scale bars are (b, d, f, h, j, l) 500 nm, (c, g) 200 nm, (k) 100 nm and inset of (l) 50 nm.

Replacing the biotinylated nanoplates by PEG-biotin functionalized 30-nm gold

nanospheres leads to core-satellite assemblies as shown in Figures 7e-g and Fig. S12.

Such structures have been predicted to modulate the native spatial and spectral

plasmonic properties of the core nanoplates.[19, 56] The decoration of the nanoplates by

the nanospheres occurs preferentially on both basal (111) facets but structure with a

core decahedron or icosahedron are also easily identified. No core-satellite structure is

formed upon incubation of streptavidinylated☐αRep gold nanocrystals with non-

biotinylated nanospheres, which remains randomly segregated (Fig. 7h, white arrows).

Finally, we have converted the streptavidinylated αRep gold nanocrystals into catalytic

nano-platforms by adding a tertiary layer of biotin-HRP enzyme (Fig. 7i-k). HRP

catalyzes the oxidation of benzidines to form water insoluble polymer aggregates. Here,

we show that the HRP-tagged gold nanocrystals trigger the polymerization of 1 mM 3,3'-

diaminobenzidine (DAB), in the presence of H_2O_2.[57] Since the catalytic reaction occurs

locally at the nanocrystal surface, a uniform layer of polymerized DAB is grown around

the nanocrystals as seen in Fig. 7j,k and Figs. S13a,b. The thickness can be adjusted

by the amount of DAB or the reaction time and is about 25 nm in the displayed sample.

When simply streptavidinylated□αRep gold nanocrystals are used, no polymerization

reaction takes place and the surface of the nanostructures remains free of polymer

over-coating (Fig. 7l). This form of catalysis reflects the stability of the

Au / αRep /enzyme construction as no side polymer particles were found in the sample,

away from the nanocrystals as it should have been expected if HRP had been grafted to

αRep loosely bound to the Au surface. The local production of polymer near plasmonic

structures allows to tune the local dielectric constant, to envision embedding more

complex optically active moieties[58] and could be harnessed for sensing applications.[59]

Conclusions

The design and combinatorial selection of fully folded artificial proteins is applied here

for the first time to the construction of crystal habit modifiers able to shape noble metals

such as gold at the nanoscale. Nine new Au(111) binding proteins have been isolated,

sequenced, mass produced and used as habit modifiers in a gold nanocrystal seeded

growth synthesis. All proteins demonstrated a high chemical affinity for gold and

structural selectivity for (111) facets, which result in an effective morphosynthetic action

yielding > 85% of (111)-terminated Au nanoplates, icosahedra and decahedra. The thin

nanoplate size could be tuned up to 500 nm that requires the recruitment of thousands

of proteins per crystalline facet. The detailed structural characterization of the

nanocrystals has established the crystalline structure of the gold nanoparticles and the

functional activity of the capping protein layer. We further demonstrated the benefit of

the artificial protein coating by derivatizing them with streptavidin, biotin and HRP

enzyme therefore incorporating extra surface functionalities such as self-assembling or

on-surface catalytic capabilities. Our approach presents several assets compared to the

design of gold-binding peptides or antibodies fragments and hence offers a promising

generic tool for the rational morphosynthesis of high-index facet nanocrystals with

superior biocompatibility and versatile *in-situ* construction of (bio)molecular platforms at

the solid interface, which could be capitalized towards plasmon-based optical devices[51, 55] and (bio-) molecular sensing applications [60-62] on individual or 2D/3D arrayed

nanoparticles.[35].

Methods

Selection of Au(111)-binding αRep proteins. αRep proteins exhibiting binding affinity

to Au(111) coated mica substrate are selected by phage display. Typically, (111)-

oriented Au films are produced by thermal evaporation on freshly cleaved mica slides

according to a well-established procedure. The protein library 2.1 comprising 1.7×10^9

variants of αRep proteins fused with phage coat protein pIII is exposed to the Au(111)

film at pH 7.5 and room temperature (r. t.).[34] Phages from the library are loaded on a

96-well Elisa plate exposing the Au(111) surface using the MicroArrayIt system

(www.arrayit.com) and incubated for 2 h at 20°C and 300 rpm. Non-specific phages are

removed by ten TBS 0.05% Tween 20 and ten TBS washing steps. Bound phages are

eluted in a glycine solution (0.1 M pH 2.5) for 10 min at 20°C and recovered by infecting

a suspension of growing XL1blue MRF' bacteria. This selection round is performed 3

times. 96 clones are analyzed by ELISA Soluble bacterial extracts are incubated on the

Au(111) film and specific binding is revealed by an antiflag-tag HRP-antibody. 18

positive hits from the ELISA test were sequenced and 9 different αReps were identified

and labelled A12, C4, D5, D7, F2, F5, F9, F10, G8. The expression and purification of

these proteins is performed according to a standard procedure detailed in

Supplementary Information.

Surface Plasmon Resonance (SPR) analysis. SPR data are recorded using the

ProteOn XPR36 (Bio-rad). αRep proteins are immobilized on HTG ProteOn sensor

chips until reaching a response signal around 200 RU in 10 mM phosphate buffer pH

7.5, 137 mM KCl, 2.7 mM KCl and 0.005% Tween 20. Interactions are recorded at a

100 µL/min flow rate and a 120 s contact time followed by a dissociation of 600 s with

citrate stabilized 5-nm diameter gold nanoparticles at different concentrations (10, 5,

2.5, 1.25 and 0.625 nM). The interspot signal is removed from the sensograms.

αRep stabilized Au seed synthesis. 50 µl of 20 µM αRep protein solution in 0.1 M

phosphate buffer (pH 7.5) is mixed with 10 µl aqueous solution of 20 mM sodium

formaldehyde sulfoxylate at r. t.. This solution is immediately injected into 100 µl of

2 mM $HAuCl_4$ solution under vigorous stirring at 900 rpm at r. t.. After stirring for 2 min,

the resulting red solution is left to grow for 2 hours until full completion of the reduction

process. The seed solution is stored at 4°C.

αRep mediated seeded growth of nanocrystals. The growth of αRep capped Au

nanocrystals is performed by adapting the hydroxylamine reduction method.[46] Briefly,

2.5 µl Au seeds are mixed with 20 µl of 100 µM αRep protein solution (0.1 M phosphate

buffer, pH 7.5) and diluted to a final volume of 245 µl with MilliQ water. Concomitantly,

5 µl of freshly prepared 200 mM hydroxylamine hydrochloride is injected to the seed

and αRep solution. The resulting solution is promptly injected to a series of 250 µl

$HAuCl_4$ solutions with final $[Au^{3+}]$ concentrations of 1 mM, 2 mM and 5 mM. The pH

value of the reaction mixture is adjusted to the desired values by adding aliquots of

0.1 M HCl or NaOH solutions. The final reaction volume is homogenized by stirred at

900 rpm for 2 min, followed by incubation at r. t. for 2 h. After synthesis, the final

products are washed 4 times by centrifugation at 8000 rpm for 5 min and re-suspended

in 1 mL MilliQ water in order to remove the uncoordinated αRep proteins.

Structural characterization of as-synthesized gold nanocrystals. Absorbance of as-synthesized gold nanocrystals is recorded on a Cary-5000 UV−vis NIR spectrophotometer in the range 200−1200 nm and at 600 nm/min scan rate. Structural analyses of the nanocrystals are carried out by scanning electron microscopy (SEM), transmission electron microscopy (TEM), selected area electron diffraction (SAED) and atomic force microscopy (AFM). Samples for SEM and AFM analyses are prepared by drop casting 20 µL of the nanocrystal suspension in milliQ water on an oxide-coated silicon wafer followed by overnight drying in air. FEG-SEM images are recorded on a Zeiss 1540XB system operated at 20 kV. Tapping mode AFM is conducted using a Bruker Dimension 3000 microscope. Extra topological information of the corrugation of the flat prismatic nanocrystals is obtained from non-contact AFM (nc-AFM) imaging in ultrahigh vacuum (UHV).[63] The samples are introduced in a Scienta Omicron Nanotechnology UHV-STM/nc-AFM microscope and probed with Pt-Ir coated silicon cantilevers (Nanosensors PPP-QNCHR) at 280-300 kHz resonance frequency and quality factors of 32000-40000. With an overall oscillation amplitude fixed at 5 nm, this attractive mode obviates protein distortion under the AFM tip and so provides accurate

height measurements and sub-molecular resolution on organic molecules.[64] Bright field

TEM and SAED analyses are conducted on a Philips CM20FEG TEM operated at

200 kV accelerating voltage and equipped with a Gatan CCD camera and Digital

Micrograph acquisition software. Size and shape distribution analyses of the electron

micrographs are performed by ImageJ software. Electron energy loss spectroscopy

(EELS) is carried out in a Hitachi HF3300 microscope equipped with a GIF (Gatan

Imaging Filter) Quantum. STEM-EDS was performed in a Phillips CM20FEG equipped

with a Brücker SDD detector. Samples for TEM are prepared by drop-casting and air-

drying a 10 µL droplet of aqueous suspension onto 300 mesh carbon film copper grids,

for TEM, SAED and EELS, or 10 nm thick SiO_2 membranes, for STEM-EDX.

Streptavidinylation of αRep capped nanocrystals. To integrate streptavidin to αRep-

capped gold nanocrystals, the lysine residues present in the αRep backbone are

biotinylated. 500 µl of as-synthesized and washed gold nanocrystals are mixed with

20 µl of 2 mg/ml NHS-biotin dissolved in DMF and incubated at r. t. for 2 hours.

Following incubation, the biotinylated gold nanocrystals are washed four times with a

0.01% Tween 20 solution adjusted at pH 7 to remove free NHS-biotin molecules and re-

suspended in PBST solution. 50 µl of 1 mg/ml Streptavidin solution is added to the

biotinylated, αRep-capped gold nanocrystals. The suspension is incubated at r. t. for 3

hours and subsequently washed 4 times with a 0.01% Tween 20 solution adjusted at

pH 7. The streptavidin-coupled gold nanocrystals assemblies are stored at 4°C.

Synthesis and PEGylation of 15-nm citrate stabilized Au nanospheres. Citrate

stabilised gold nanospheres (AuNP) are synthesised using Turkevich's method.[65]

Briefly, 20 ml of 0.25 mM $HAuCl_4$ solution is heated to boiling point prior to the rapid

addition of 120 µl of a 50 mg/ml sodium citrate solution under vigorous stirring. The

solution is continuously stirred for 30 min, until it turns to ruby red. The AuNP

suspension is allowed to cool down at RT over 4 hours. 2 ml of AuNP suspension are

centrifuged at 14,500 rpm for 15 min. The supernatant is discarded and the pellet is re-

suspended in 500 µl of a 2 mg/ml biotin-PEG-SH solution and incubated for 6 h.

PEGylated AuNP are washed eight times with MilliQ water at 14,500 rpm for 15 min

and, finally, re-suspended in 100 µl MilliQ water before storage at 4°C.

Peroxidase-catalyzed 3,3' diaminobenzidine polymerization. A 2 mg/ml solution of

horseradish peroxidase (HRP) in PBS buffer is mixed with 20 µl of a 2 mg/ml NHS-biotin

dissolved in DMF. Biotinylation of HRP is allowed to proceed for 2 h. Excess NHS-biotin

is removed by passing thee solution through a Zepa spin desalting column

(Thermofisher Scientific). Next, 500 µl of streptavidinylated, αRep-capped gold

nanocrystals are reacted with biotinylated HRP enzyme at RT for 2 h. The HRP-coupled

gold nanocrystals are washed four times at 8,000 rpm for 5 min with a 0.01% Tween 20

solution adjusted at pH 7 to eliminate unconjugated biotin-HRP. 5 µl of HRP-gold

nanocrystals are drop-casted on silicon substrates and allowed to dry for 3 hrs.

Enzyme-catalyzed polymerisation and precipitation (ECPP)[66] of 3,3'-diaminobenzidine

(DAB) is triggered locally by drop-casting 30 µl of a freshly prepared 1 mM aqueous

solution of DAB on top of the silicon-immobilized HRP-gold nanocrystals, in the

presence of 5 µl 30%w/w H_2O_2 solution. The DAB polymerization reaction by HRP is

allowed to proceed for 3 h. Finally, the silicon substrate is washed 6 times with 100 µl of

MilliQ water and air dried.

ASSOCIATED CONTENT

Supporting Information.

The following files are available free of charge. Materials and Methods. Screening and

biochemical characterization of αRep (Fig. S1). Determination of Au(111)] binding

affinities (Figs. S2a-d). TEM and gel electrophoresis on AU seeds (Fig. S3). Two-stage

seeded growth details (Fig. S4). SEM characterization of αRep coated Au nanocrystals

(Fig. S5). UV-visible spectral characterization (Fig. S6). Control experiments with non-

selected αRep (Fig. S7). Au nanocrystal size tenability (Fig.S8). Effect of pH (Fig; S9)

and temperature (Fig. S10). Chemical analysis of G8-capped nanocrystals (Fig.S11).

SEM images of core-satellite self-assembled nanostructures (Fig.S12). SEM images of

in-situ DAB encapsulated Au nanocrystals (Fig.S13a,b). (PDF)

AUTHOR INFORMATION

Corresponding Authors

* Erik.Dujardin@cemes.fr, Philippe.Minard@i2bc.paris-saclay.fr

Table of Content illustration
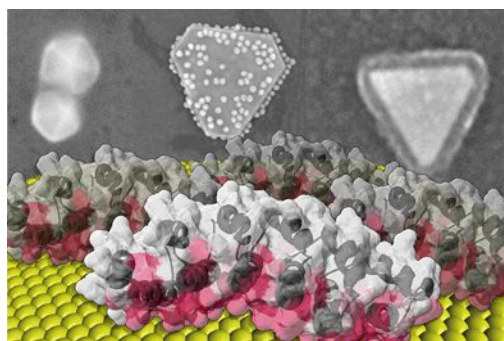
REFERENCES

1.   Williams, M.; Daviter, T., *Protein-Ligand Interactions. Methods and Applications.* Humana Press: New York, 2013.

2.   Mann, S., *Biomineralization. Principles and Concepts in Bioinorganic Materials Chemistry.* Oxford University Press: Oford, 2001.

3.   Wilt, F. H., Developmental biology meets materials science: Morphogenesis of biomineralized structures. *Dev. Biol.* **2005,** *280* (1), 15-25.

4.   Peisajovich, S. G.; Tawfik, D. S., Protein engineers turned evolutionists. *Nat. Methods* **2007,** *4* (12), 991-994.

5.   Packer, M. S.; Liu, D. R., Methods for the directed evolution of proteins. *Nat. Rev. Genet.* **2015,** *16* (7), 379-394.

6.   Brown, S., Metal-recognition by repeating polypeptides. *Nat. Biotechnol.* **1997,** *15* (3), 269-272.

7.   Whaley, S. R.; English, D. S.; Hu, E. L.; Barbara, P. F.; Belcher, A. M., Selection of peptides with semiconductor binding specificity for directed nanocrystal assembly. *Nature* **2000,** *405* (6787), 665-668.

8.   Lee, S. W.; Mao, C. B.; Flynn, C. E.; Belcher, A. M., Ordering of quantum dots using genetically engineered viruses. *Science* **2002,** *296* (5569), 892-895.

9.   Sarikaya, M.; Tamerler, C.; Jen, A. K. Y.; Schulten, K.; Baneyx, F., Molecular biomimetics: nanotechnology through biology. *Nat. Mater.* **2003,** *2* (9), 577-585.

10.   Vallee, A.; Humblot, V.; Pradier, C. M., Peptide Interactions with Metal and Oxide Surfaces. *Accounts Chem. Res.* **2010,** *43* (10), 1297-1306.

11.   Nam, K. T.; Kim, D. W.; Yoo, P. J.; Chiang, C. Y.; Meethong, N.; Hammond, P. T.; Chiang, Y. M.; Belcher, A. M., Virus-enabled synthesis and assembly of nanowires for lithium ion battery electrodes. *Science* **2006,** *312* (5775), 885-888.

12.   Chiu, C.-Y.; Li, Y.; Ruan, L.; Ye, X.; Murray, C. B.; Huang, Y., Platinum nanocrystals selectively shaped using facet-specific peptide sequences. *Nature Chemistry* **2011,** *3* (5), 393-399.

13.   So, C. R.; Kulp, J. L.; Oren, E. E.; Zareie, H.; Tamerler, C.; Evans, J. S.; Sarikaya, M., Molecular Recognition and Supramolecular Self-Assembly of a

Genetically Engineered Gold Binding Peptide on Au{111}. *ACS Nano* **2009,** *3* (6), 1525-1531.

14. Winter, G.; Griffiths, A. D.; Hawkins, R. E.; Hoogenboom, H. R., Making antibodies by phage display technology. *Annu. Rev. Immunol.* **1994,** *12*, 433-455.

15. Buss, N.; Henderson, S. J.; McFarlane, M.; Shenton, J. M.; de Haan, L., Monoclonal antibody therapeutics: history and future. *Curr. Opin. Pharmacol.* **2012,** *12* (5), 615-622.

16. Soshee, A.; Zurcher, S.; Spencer, N. D.; Halperin, A.; Nizak, C., General In Vitro Method to Analyze the Interactions of Synthetic Polymers with Human Antibody Repertoires. *Biomacromolecules* **2014,** *15* (1), 113-121.

17. Artzy Schnirman, A.; Zahavi, E.; Yeger, H.; Rosenfeld, R.; Benhar, I.; Reiter, Y.; Sivan, U., Antibody Molecules Discriminate between Crystalline Facets of a Gallium Arsenide Semiconductor. *Nano Letters* **2006,** *6* (9), 1870-1874.

18. Hattori, T.; Umetsu, M.; Nakanishi, T.; Sawai, S.; Kikuchi, S.; Asano, R.; Kumagai, I., A High-Affinity Gold-Binding Camel Antibody: Antibody Engineering for One-Pot Functionalization of Gold Nanoparticles as Biointerface Molecules. *Bioconjugate Chem.* **2012,** *23* (9), 1934-1944.

19. Jain, P.; Soshee, A.; Narayanan, S. S.; Sharma, J.; Girard, C.; Dujardin, E.; Nizak, C., Selection of Arginine-Rich Anti-Gold Antibodies Engineered for Plasmonic Colloid Self-Assembly. *J. Phys. Chem. C* **2014,** *118* (26), 14502-14510.

20. Xie, J.; Lee, J. Y.; Wang, D. I. C., Synthesis of Single-Crystalline Gold Nanoplates in Aqueous Solutions through Biomineralization by Serum Albumin Protein. *The Journal of Physical Chemistry C* **2007,** *111* (28), 10226-10232.

21. Kim, J.; Rheem, Y.; Yoo, B.; Chong, Y.; Bozhilov, K. N.; Kim, D.; Sadowsky, M. J.; Hur, H.-G.; Myung, N. V., Peptide-mediated shape- and size-tunable synthesis of gold nanostructures. *Acta Biomaterialia* **2010,** *6* (7), 2681-2689.

22. Darnell, M.; Mooney, D. J., Leveraging advances in biology to design biomaterials. *Nat. Mater.* **2017,** *16* (12), 1178-1185.

23. Voet, A. R. D.; Tame, J. R. H., Protein-templated synthesis of metal-based nanomaterials. *Curr. Opin. Biotechnol.* **2017,** *46*, 14-19.

24. Liu, Y.; Guo, R., Synthesis of protein–gold nanoparticle hybrid and gold nanoplates in protein aggregates. *Materials Chemistry and Physics* **2011,** *126* (3), 619-627.

25. Li, C.; Bolisetty, S.; Mezzenga, R., Hybrid Nanocomposites of Gold Single-Crystal Platelets and Amyloid Fibrils with Tunable Fluorescence, Conductivity, and Sensing Properties. *Adv. Mater.* **2013,** *25* (27), 3694-3700.

26. Cantaert, B.; Ding, D.; Rieu, C. m.; Petrone, L.; Hoon, S.; Kock, K. H.; Miserez, A., Stable Formation of Gold Nanoparticles onto Redox-Active Solid Biosubstrates Made of Squid Suckerin Proteins. *Macromol. Rapid Commun.* **2015,** *36* (21), 1877-1883.

27. Liu, B.; Xie, J.; Lee, J. Y.; Ting, Y. P.; Chen, J. P., Optimization of High-Yield Biological Synthesis of Single-Crystalline Gold Nanoplates. *The Journal of Physical Chemistry B* **2005,** *109* (32), 15256-15263.

28. Shankar, S. S.; Rai, A.; Ankamwar, B.; Singh, A.; Ahmad, A.; Sastry, M., Biological synthesis of triangular gold nanoprisms. *Nat. Mater.* **2004,** *3* (7), 482-488.

29. Binz, H. K.; Amstutz, P.; Pluckthun, A., Engineering novel binding proteins from nonimmunoglobulin domains. *Nat. Biotechnol.* **2005,** *23* (10), 1257-1268.

30. Boersma, Y. L.; Pluckthun, A., DARPins and other repeat protein scaffolds: advances in engineering and applications. *Curr. Opin. Biotechnol.* **2011,** *22* (6), 849-857.

31. Urvoas, A.; Valerio-Lepiniec, M.; Minard, P., Artificial proteins from combinatorial approaches. *Trends in Biotechnology* **2012,** *30* (10), 512-520.

32. Parmeggiani, F.; Huang, P. S., Designing repeat proteins: a modular approach to protein design. *Curr. Opin. Struct. Biol.* **2017,** *45*, 116-123.

33. Urvoas, A.; Guellouz, A.; Valerio-Lepiniec, M.; Graille, M.; Durand, D.; Desravines, D. C.; van Tilbeurgh, H.; Desmadril, M.; Minard, P., Design, Production and Molecular Structure of a New Family of Artificial Alpha-helicoidal Repeat Proteins (Î±Rep) Based on Thermostable HEAT-like Repeats. *Journal of Molecular Biology* **2010,** *404* (2), 307-327.

34. Guellouz, A.; Valerio-Lepiniec, M.; Urvoas, A.; Chevrel, A.; Graille, M.; Fourati-Kammoun, Z.; Desmadril, M.; van Tilbeurgh, H.; Minard, P., Selection of Specific

Protein Binders for Pre-Defined Targets from an Optimized Library of Artificial Helicoidal Repeat Proteins (alphaRep). *PLoS One* 2013, *8* (8), e71512.

35.   Gurunatha, K. L.; Fournier, A. C.; Urvoas, A.; Valerio-Lepiniec, M.; Marchi, V.; Minard, P.; Dujardin, E., Nanoparticles Self-Assembly Driven by High Affinity Repeat Protein Pairing. *ACS Nano* 2016, *10* (3), 3176-3185.

36.   Mejias, S. H.; Lopez-Andarias, J.; Sakurai, T.; Yoneda, S.; Erazo, K. P.; Seki, S.; Atienza, C.; Martin, N.; Cortajarena, A. L., Repeat protein scaffolds: ordering photo- and electroactive molecules in solution and solid state. *Chemical Science* 2016, *7* (8), 4842-4847.

37.   Chevrel, A.; Mesneau, A.; Sanchez, D.; Celma, L.; Quevillon-Cheruel, S.; Cavagnino, A.; Nessler, S.; de la Sierra-Gallay, I. L.; van Tilbeurgh, H.; Minard, P.; Valerio-Lepiniec, M.; Urvoas, A., Alpha repeat proteins (alpha Rep) as expression and crystallization helpers. *J. Struct. Biol.* 2018, *201* (2), 88-99.

38.   Chevrel, A.; Urvoas, A.; de la Sierra-Gallay, I. L.; Aumont-Nicaise, M.; Moutel, S.; Desmadril, M.; Perez, F.; Gautreau, A.; van Tilbeurgh, H.; Minard, P.; Valerio-Lepiniec, M., Specific GFP-binding artificial proteins (alpha Rep): a new tool for in vitro to live cell applications. *Biosci. Rep.* 2015, *35*, e00223.

39.   Hadpech, S.; Nangola, S.; Chupradit, K.; Fanhchaksai, K.; Furnon, W.; Urvoas, A.; Valerio-Lepiniec, M.; Minard, P.; Boulanger, P.; Hong, S. S.; Tayapiwatana, C., Alpha-helicoidal HEAT-like Repeat Proteins (alpha Rep) Selected as Interactors of HIV-1 Nucleocapsid Negatively Interfere with Viral Genome Packaging and Virus Maturation. *Scientific Reports* 2017, *7*, 16335.

40.   Willett, R. L.; Baldwin, K. W.; West, K. W.; Pfeiffer, L. N., Differential adhesion of amino acids to inorganic surfaces. *Proc. Natl. Acad. Sci. U. S. A.* 2005, *102* (22), 7817-7822.

41.   Calzolari, A.; Cicero, G.; Cavazzoni, C.; Di Felice, R.; Catellani, A.; Corni, S., Hydroxyl-Rich beta-Sheet Adhesion to the Gold Surface in Water by First-Principle Simulations. *Journal of the American Chemical Society* 2010, *132* (13), 4790-4795.

42.   Hoefling, M.; Iori, F.; Corni, S.; Gottschalk, K. E., Interaction of Amino Acids with the Au(111) Surface: Adsorption Free Energies from Molecular Dynamics Simulations. *Langmuir* 2010, *26* (11), 8347-8351.

43. Feng, J.; Pandey, R. B.; Berry, R. J.; Farmer, B. L.; Naik, R. R.; Heinz, H., Adsorption mechanism of single amino acid and surfactant molecules to Au {111} surfaces in aqueous solution: design rules for metal-binding molecules. *Soft Matter* **2011,** *7* (5), 2113-2120.

44. Johnson, C. L.; Snoeck, E.; Ezcurdia, M.; Rodriguez-Gonzalez, B.; Pastoriza-Santos, I.; Liz-Marzan, L. M.; Hytch, M. J., Effects of elastic anisotropy on strain distributions in decahedral gold nanoparticles. *Nat. Mater.* **2008,** *7* (2), 120-124.

45. Khanna, P. K.; Gokhale, R.; Subbarao, V. V. V. S.; Vishwanath, A. K.; Das, B. K.; Satyanarayana, C. V. V., PVA stabilized gold nanoparticles by use of unexplored albeit conventional reducing agent. *Materials Chemistry and Physics* **2005,** *92* (1), 229-233.

46. Brown, K. R.; Natan, M. J., Hydroxylamine Seeding of Colloidal Au Nanoparticles in Solution and on Surfaces. *Langmuir* **1998,** *14* (4), 726-728.

47. Scarabelli, L.; Sánchez-Iglesias, A.; Pérez-Juste, J.; Liz-Marzán, L. M., A "Tips and Tricks" Practical Guide to the Synthesis of Gold Nanorods. *The Journal of Physical Chemistry Letters* **2015,** *6* (21), 4270-4279.

48. Viarbitskaya, S.; Teulle, A.; Cuche, A.; Sharma, J.; Girard, C.; Dujardin, E.; Arbouet, A., Morphology-induced redistribution of surface plasmon modes in two-dimensional crystalline gold platelets. *Appl. Phys. Lett.* **2013,** *103* (13).

49. Jin, R.; Cao, Y.; Mirkin, C. A.; Kelly, K. L.; Schatz, G. C.; Zheng, J. G., Photoinduced Conversion of Silver Nanospheres to Nanoprisms. *Science* **2001,** *294* (5548), 1901.

50. Chen, L.; Ji, F.; Xu, Y.; He, L.; Mi, Y.; Bao, F.; Sun, B.; Zhang, X.; Zhang, Q., High-Yield Seedless Synthesis of Triangular Gold Nanoplates through Oxidative Etching. *Nano Letters* **2014,** *14* (12), 7201-7206.

51. Viarbitskaya, S.; Teulle, A.; Marty, R.; Sharma, J.; Girard, C.; Arbouet, A.; Dujardin, E., Tailoring and imaging the plasmonic local density of states in crystalline nanoprisms. *Nature Materials* **2013,** *12* (5), 426-432.

52. Millstone, J. E.; Metraux, G. S.; Mirkin, C. A., Controlling the edge length of gold nanoprisms via a seed-mediated approach. *Adv. Funct. Mater.* **2006,** *16* (9), 1209-1214.

53. Brown, S.; Sarikaya, M.; Johnson, E., A genetic analysis of crystal growth. *Journal of Molecular Biology* **2000,** *299* (3), 725-735.

54. Bolisetty, S.; Vallooran, J. J.; Adamcik, J.; Handschin, S.; Gramm, F.; Mezzenga, R., Amyloid-mediated synthesis of giant, fluorescent, gold single crystals and their hybrid sandwiched composites driven by liquid crystalline interactions. *Journal of Colloid and Interface Science* **2011,** *361* (1), 90-96.

55. Haberfehlner, G.; Schmidt, F. P.; Schaffernak, G.; Horl, A.; Trugler, A.; Hohenau, A.; Hofer, F.; Krenn, J. R.; Hohenester, U.; Kothleitner, G., 3D Imaging of Gap Plasmons in Vertically Coupled Nanoparticles by EELS Tomography. *Nano Letters* **2017,** *17* (11), 6773-6777.

56. Cuche, A.; Viarbitskaya, S.; Sharma, J.; Arbouet, A.; Girard, C.; Dujardin, E., Modal engineering of Surface Plasmons in apertured Au Nanoprisms. *Scientific Reports* **2015,** *5*.

57. Chen, S.; Svedendahl, M.; Van Duyne, R. P.; Käll, M., Plasmon-Enhanced Colorimetric ELISA with Single Molecule Sensitivity. *Nano Letters* **2011,** *11* (4), 1826-1830.

58. Gather, M. C.; Meerholz, K.; Danz, N.; Leosson, K., Net optical gain in a plasmonic waveguide embedded in a fluorescent polymer. *Nat. Photonics* **2010,** *4* (7), 457-461.

59. Rodriguez-Lorenzo, L.; de la Rica, R.; Alvarez-Puebla, R. A.; Liz-Marzan, L. M.; Stevens, M. M., Plasmonic nanosensors with inverse sensitivity by means of enzyme-guided crystal growth. *Nat. Mater.* **2012,** *11* (7), 604-607.

60. Beeram, S. R.; Zamborini, F. P., Selective Attachment of Antibodies to the Edges of Gold Nanostructures for Enhanced Localized Surface Plasmon Resonance Biosensing. *Journal of the American Chemical Society* **2009,** *131* (33), 11689-11691.

61. Nuraje, N.; Mohammed, S.; Yang, L.; Matsui, H., Biomineralization Nanolithography: Combination of Bottom-Up and Top-Down Fabrication To Grow Arrays of Monodisperse Gold Nanoparticles Along Peptide Lines. *Angewandte Chemie International Edition* **2009,** *48* (14), 2546-2548.

62. Qin, F.; Zhao, T.; Jiang, R.; Jiang, N.; Ruan, Q.; Wang, J.; Sun, L.-D.; Yan, C.-H.; Lin, H.-Q., Thickness Control Produces Gold Nanoplates with Their Plasmon in the Visible and Near-Infrared Regions. *Advanced Optical Materials* **2016,** *4* (1), 76-85.

63.   Baris, B.; Alchaar, M.; Prasad, J.; Gauthier, S.; Dujardin, E.; Martrou, D., Controlling the electric charge of gold nanoplatelets on an insulator by field emission nc-AFM. *Appl. Phys. Lett.* **2018,** *112* (11).

64.   Cerreta, A.; Vobornik, D.; Dietler, G., Fine DNA structure revealed by constant height frequency modulation AFM imaging. *Eur. Polym. J.* **2013,** *49* (8), 1916-1922.

65.   Turkevich, J.; Stevenson, P. C.; Hillier, J., The formation of colloidal gold. *J. Phys. Chem.* **1953,** *57* (7), 670-673.

66.   Klibanov, A. M.; Tu, T.-M.; Scott, K. P., Peroxidase-Catalyzed Removal of Phenols from Coal-Conversion Waste Waters. *Science* **1983,** *221* (4607), 259.
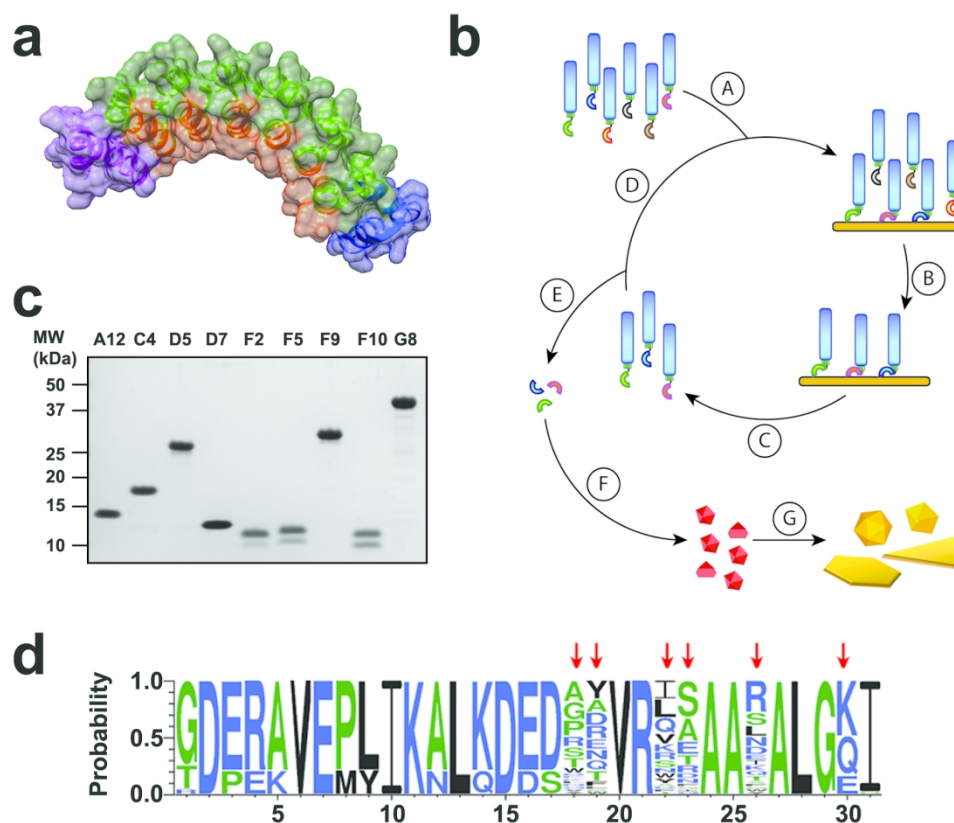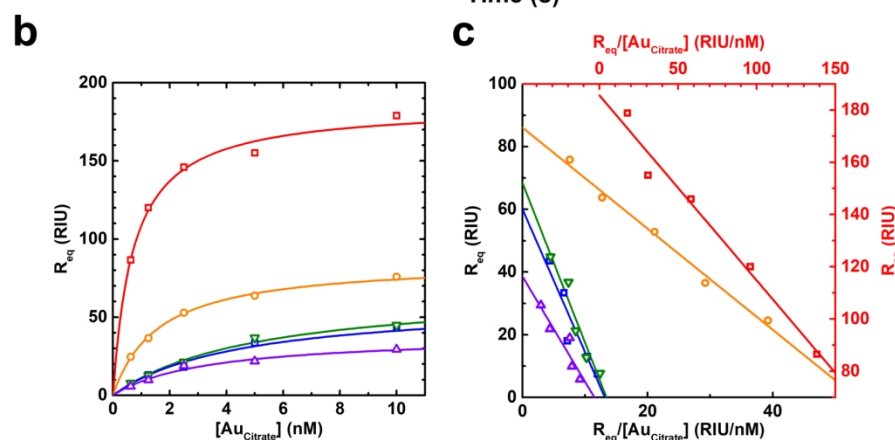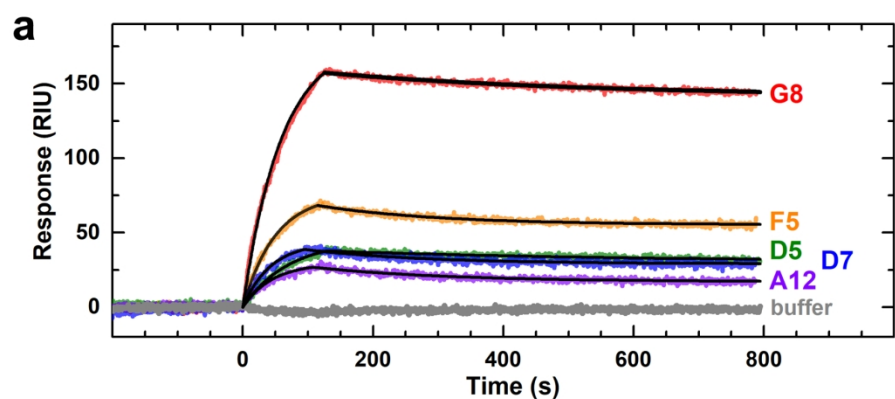
Figure 1. Construction and directed evolution of Au(111)-binding artificial repeat proteins. (a) 3D representation of the crystallographic structure of a 4-repeat αRep protein depicting the internal repeats comprising the hypervariable positions (brown) with their conserved scaffold regions (green), N- and C-cap (blue). (b) Schematic flowchart showing the phage display design and selection of αRep's (A-D) and the ☐Rep directed Au nanocrystal morphosynthesis (I-J) process. These steps involve: (A) Construction of the phage display library; (B) ☐Rep selection on planar Au(111) substrate on mica and elution of unbound phage at pH5; (D) acid elution of Au-bound phages and bacterial amplification of selected phages (E) proteolytic isolation of αRep from phage body and large scale production. The morphosynthesis of Au nanocrystals by seeded growth process comprises: (F) αRep directed Au seed synthesis; (G) nanocrystal growth in the presence of excess αRep through hydroxylamine-mediated disproportionation mechanism. (c) Coomassie blue stained SDS-PAGE profiles of 9 different Au(111)-selected ☐Rep after cleavage digestion. The position of the major bands represents the molecular weight of respective αRep. (d) Sequence logo obtained by multi-alignment of the sequences of all the repeats from the selected αRep, including those of the N-cap that have the same second helix as the internal repeats, hence the apparent variability observed in positions (1,3,4,8,9,12,14,17). The binding hypervariable surface is generated by the position indicated by red arrows.

Figure 2. Gold affinity of the selected anti-Au(111) repeat proteins. (a) SPR sensograms during adsorption and desorption phases monitoring the interactions between immobilized αRep proteins (see labels) and citrate-stabilized Au nanoparticles ([Aucit]=10 nM). Solid black lines are exponential fits to the association and dissociation phases. The exponent of the association fits provides the association (kON) and dissociation (kOFF #1) kinetic constants tabulated in (d). The dissociation phase fits provide the kOFF #2 kinetic constant in Table (d). Each protein data is associated to the same color throughout the figure. (b) SPR equilibrium analysis along with Langmuir fits (continuous lines). (c) Scatchard plot for the empirical estimation of the dissociation constants labelled KD #3 which is obtained from the slopes of the linear fits. G8 data (red) are plotted on the red x-y axis while all other data share the black x-y axis. (d) Summary table of all association (kON) and dissociation (kOFF #1 and kOFF #2) alongside the dissociation constant (KD) values obtained from the ratio of kinetic constants (KD#1= kOFF #1 / kON, KD#2= kOFF #2 / kON) and from the Scatchard plot (KD#3).
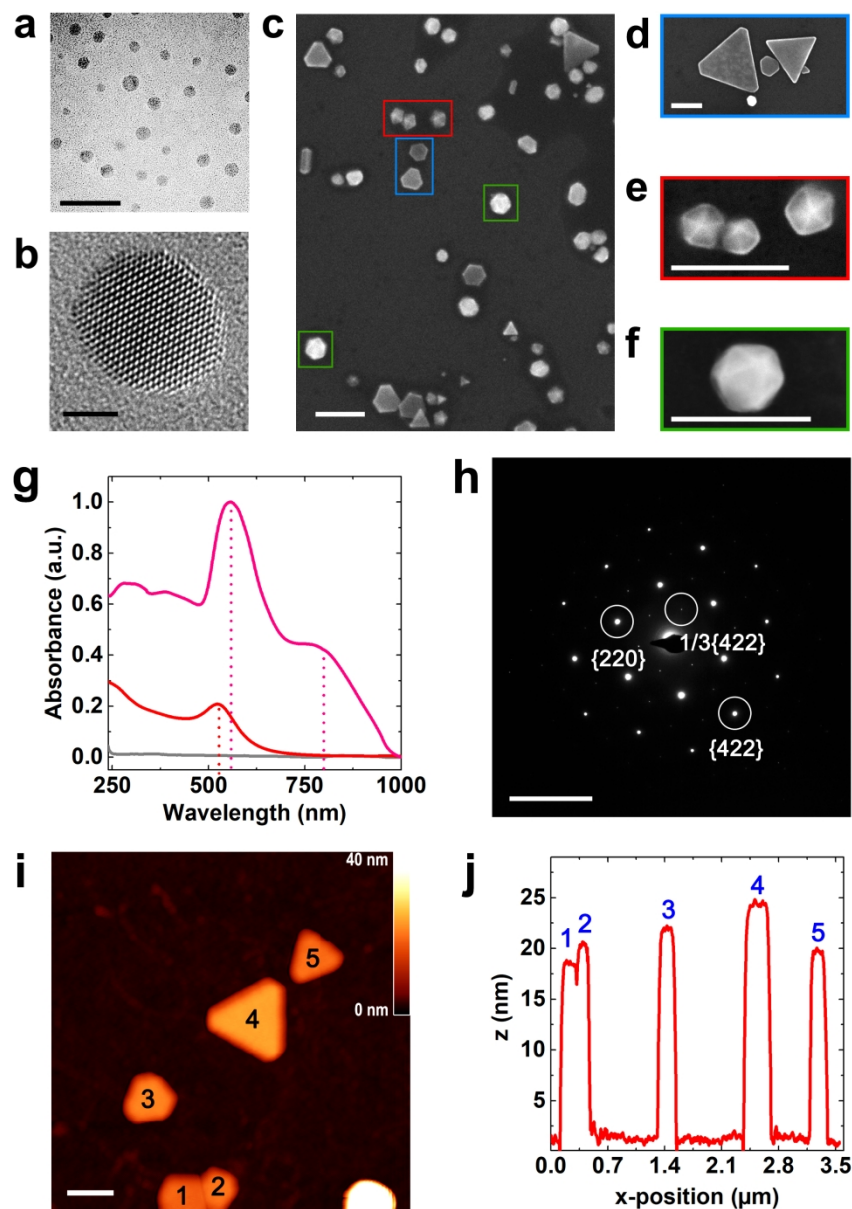
Figure 3. Morphological and structural characterization of αRep-coated, (111)-terminated Au nanocrystals. (a,b) High resolution TEM of spherical G8-stabilized seeds showing a high degree of crystallinity. The seed in (b) is single crystalline and oriented along the [011] zone axis (c) Representative SEM micrograph of G8-capped, (111)-facet terminated Au nanostructures showing nanoplates (blue box), decahedrons (red box) and icosahedrons (green box) morphologies. (g) Characteristic UV-visible spectra of G8 templated Au seeds (red, λmax = 524 nm), seedless growth solution (grey) and Au nanostructures synthesized by the G8-templated, seeded growth approach (pink), which exhibit two peaks at λmax = 556 nm and λmax = 804 nm. (h) Selected area electron diffraction of an Au nanoplate showing diffraction spots along the [111] zone axis. (i) Tapping mode AFM image of five Au nanoplates. (j) Height profile of the five nanoplates shown in (i), which all have a thickness of 21 ± 3 nm. Scale bars are (a) 20 nm, (b) 2 nm, (c-f, i) 200 nm, (h) 10 nm-1.
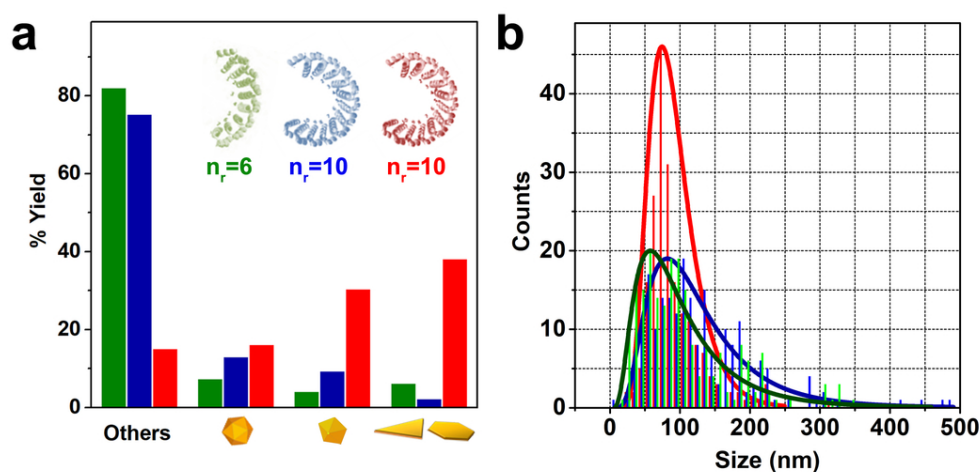
Figure 4: Comparative analysis of nanocrystal shapes and sizes obtained in the presence of control proteins, anti-GFP and N10, or anti-Au(111) G8. (a) Histogram showing the relative occurrence of nanoprisms, decahedra, icosahedra and other shape (spheroidal, and irregular shapes) obtained by morphosynthesis with anti-GFP □Rep (green), of consensus sequence N10 αRep (blue) and the isomorphic anti-Au(111) G8 αRep (red). (b) Size distribution histograms and log-normal fits of as-synthesized nanocrystals with anti-GFP (green), N10 (blue) and G8 (red) αRep proteins (200 measurements for each set).
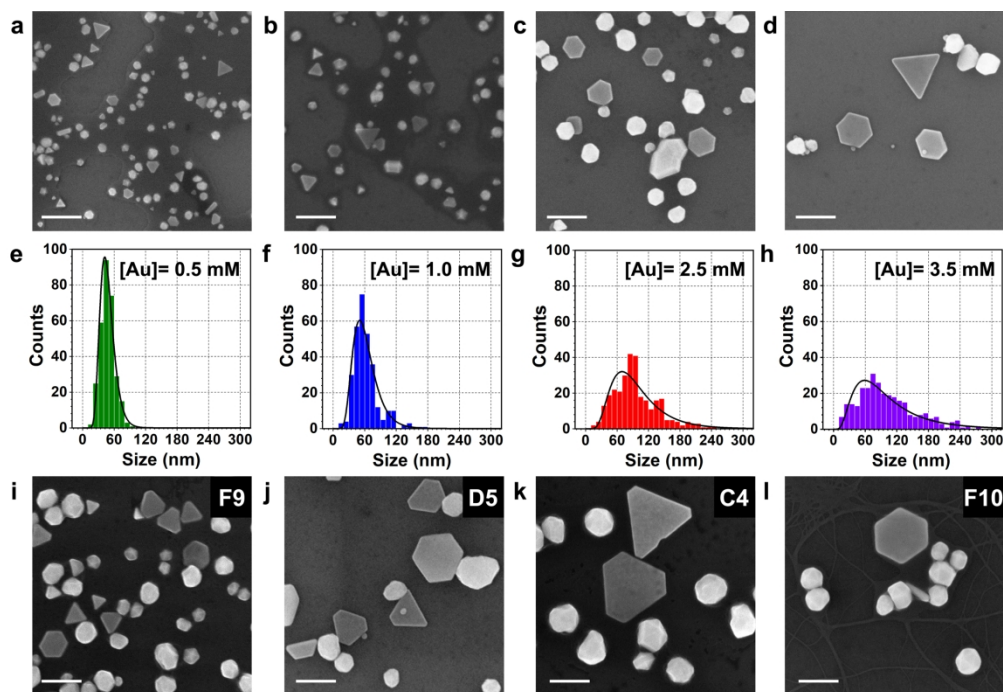
90x50mm (300 x 300 DPI)

Figure 5: Nanocrystal size adjustment by varying the initial Au3+ concentration and generalized synthesis with other selected proteins. (a-h) SEM micrographs and nanocrystal size distribution of kinetically controlled G8-capped Au nanostructures for four different Au3+ concentrations: (a, e) 0.5 mM; (b,f) 1.0 mM; (c,g) 2.5 mM; (d, h) 3.5 mM. The histograms follow lognormal distributions (black lines) with sizes of (e) 48±14 nm, (f) 62±24 nm, (g) 99±50 nm and (h) 105±72 nm. (i-l) SEM micrographs of nanostructures synthesized in the presence of different αRep at the same Au3+ concentration of 2.5 mM: (i) F9; (j) D5; (k) C4; (l) F10. Scale bars: 200 nm.
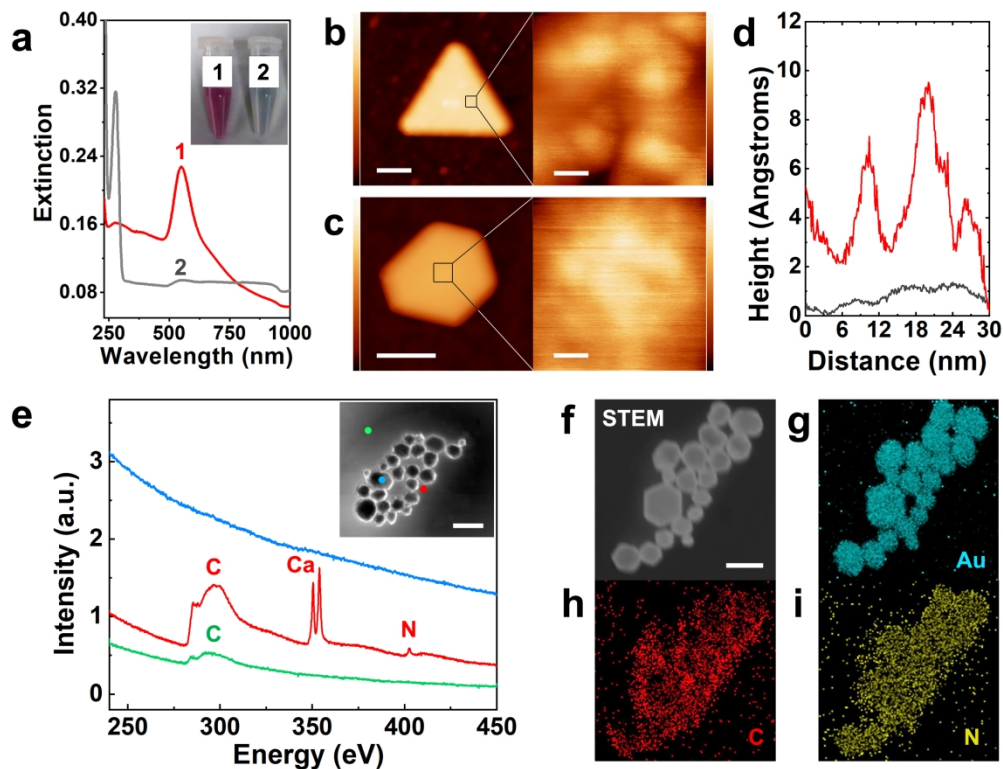
Figure 6: Chemical analysis of the αRep-Au interface on the surface of the G8-coated nanocrystals. (a) Trypsinization test on G8-capped nanocrystals monitored by UV-visible spectrometry. Sample in tube1 consists in stable nanocrystals produced with G8 that show a clear plasmon resonance at 520 nm (spectrum 1). In tube 2, trypsin is used to degrade the protein shell resulting in nanocrystal aggregation and the disappearance of the resonance peak (spectrum 2). (b, c) nc-AFM images of (b) G8-capped and (c) O2 plasma cleaned nanoplates. The black squares indicate the areas zoomed in the right panels. Scale bars are 100 nm and 6 nm for the left and right panels respectively. (d) nc-AFM height profiles of the G8-coated triangular nanoprism (red) and of the plasma-cleaned hexagonal nanoprisms (black) shown in (b) and (c) respectively. (e) EELS spectra taken from three locations in the TEM image of streptavidinylated G8-capped nanocrystals shown in inset. The background spectrum (green) shows only the carbon peak. The blue spectrum taken at the center of a Au nanocrystal shows a large uniform background due to a very low energy Au peak located out of the spectral window. The red spectrum recorded tangentially to the nanocrystal reveals the presence of Nitrogen, Carbon, and Calcium. Note that the Ca signal is ascribed from the calcium-based purification method of commercial streptavidin. Scale bar in inset is 200 nm. (f) STEM image and (g-i) corresponding EDS maps showing elemental distribution of (g) gold (h) carbon (i) nitrogen. Scale bar in (f) is 400 nm.
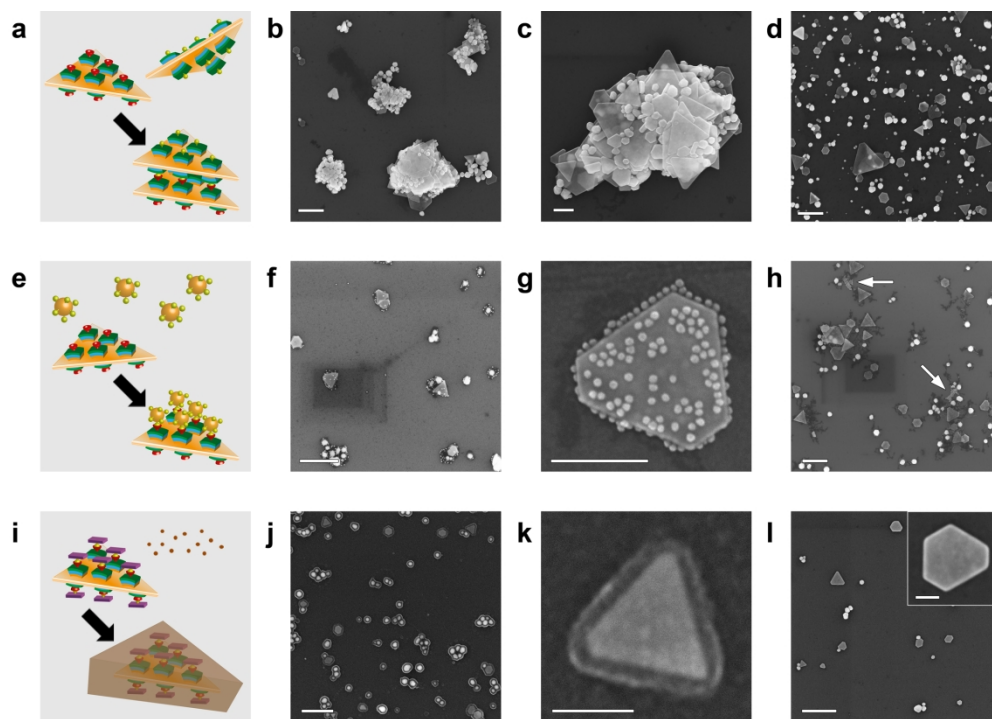
Figure 7: Functional surface derivatization of αRep protein coated nanocrystals. (a) Scheme and (b, c) SEM images of basal stacking of G8-capped Au nanocrystals obtained by self-assembly between streptavidinylated and biotinylated nanocrystals. (d) Control experiment in absence of biotin shows no stacking. (e) Scheme and (f, g) SEM images of core-satellite hybrid assemblies obtained by combining streptavidinylated G8 nanocrystals and biotin-PEG Au nanospheres which results in the decoration of the top and bottom prism facets by the nanospheres. (h) Control experiment with non- streptavidinylated G8-capped Au nanocrystals. No satellite is observed even though segregated nanosphere clumps can be found (white arrows). (i) Scheme and (j, k) SEM images of on-surface DAB catalysis by HRP-Biotin tagged streptavidinylated G8 nanocrystals results in a uniformly wrapping polymer corona. (l) Control experiment run with simply streptavidinylated nanocrystal in the absence of HRP. No polymer capping layer as shown also in the inset. Scale bars are (b, d, f, h, j, l) 500 nm, (c, g) 200 nm, (k) 100 nm and inset of (l) 50 nm.